

Banner appropriate to article type will appear here in typeset article

Focusing of concentric free-surface waves

Lohit Kayal¹, Vatsal Sanjay², Nikhil Yewale¹, Anil Kumar¹ and Ratul Dasgupta¹†

¹Chemical Engineering, Indian Institute of Technology, Bombay, India 400 076,

²Physics of Fluids Group, Max Planck Center for Complex Fluid Dynamics, Department of Science and Technology, and J. M. Burgers Centre for Fluid Dynamics, University of Twente, P. O. Box 217, 7500 AE Enschede, The Netherlands

(Received xx; revised xx; accepted xx)

Gravito-capillary waves at free-surfaces are ubiquitous in several natural and industrial processes involving quiescent liquid pools bounded by cylindrical walls. These waves emanate from the relaxation of initial interface distortions, which often take the form of a cavity (depression) centred on the symmetry axis of the container. These surface waves reflect from the container walls leading to a radially inward propagating wave-train converging (focussing) onto the symmetry axis. Under the inviscid approximation and for sufficiently shallow cavities, the relaxation is well-described by the linearised potential-flow equations. Naturally, adding viscosity to such a system introduces viscous dissipation that enervates energy and dampens the oscillations at the symmetry axis. However, for viscous liquids and deeper cavities, these equations are qualitatively inaccurate. In this study, we elucidate a modal approach to study the initial-value problem for concentric gravito-capillary waves generated on a free-surface for inviscid as well as viscous liquids. For a sufficiently deep cavity, the inward focusing of waves results in large interfacial oscillations at the axis, necessitating a second-order nonlinear theory. We demonstrate that this theory effectively models the interfacial behavior and highlights the crucial role of nonlinearity near the symmetry axis. Contrary to expectations, the addition of slight viscosity further intensifies the oscillations at the symmetry axis. This finding underscores the limitations of the potential flow model and suggests avenues for more accurate modelling of such complex free-surface flows.

Key words: Surface waves, nonlinear waves, jet formation, wave focussing, Cauchy-Poisson problem, viscous waves

1. Introduction to wave focussing

Focusing of moderate amplitude, progressive surface waves can often in turn produce unexpectedly large waves. At oceanic scales, spatial wave focusing, where large amplitude waves form persistently in specific regions (Torres *et al.* 2022; Chavarria *et al.* 2018), can produce waves powerful enough to damage or capsize ships. A famous example is the Aghulas

† Email address for correspondence: dasgupta.ratul@gmail.com

current region (Britannica, The Editors of Encyclopaedia 2024) known for giant waves and shipping accidents (Mallory 1974; Smith 1976). The role of current generated refractive focusing of waves leading to the birth of such giant waves, specifically in the Agulhas, was anticipated by Peregrine (1976) (also see fig. 8 in Dysthe *et al.* (2008) and section 2 in White & Fornberg (1998)). Refractive focusing of surface waves (Peregrine 1986) has also been exploited to design ‘lenses’ i.e., submerged structures in a water basin which focus incoming divergent, circular waves (see fig. 1a in Stamnes *et al.* (1983)), these being motivated from wave generation of power (McIver 1985; Murashige & Kinoshita 1992).

In addition to *spatial focusing*, *spatio-temporal focusing* also occurs (Dysthe *et al.* 2008), where large wave amplitudes manifest at specific locations in space, albeit briefly. Spatio-temporal focussing has obvious relevance not only towards understanding, for example, rogue (freak) waves in the ocean (Charlie Wood 2020) but also to our current study (next section). The physical mechanisms underlying spatio-temporal focussing have been distinguished further into *linear* and *nonlinear* dispersive focusing (section 4.2, 4.3, Dysthe *et al.* (2008)). Linear dispersive focussing of progressive waves relies on constructive interference exploiting the dispersive nature of surface gravity waves and is particularly simple to understand in the deep water limit. For uni-directional wave packets in deep water, generated from a wavemaker oscillating harmonically at frequency Ω at one end of a sufficiently long wave flume, the energy propagation velocity (group velocity) of the packet is $c_g = \frac{g}{2\Omega}$ where g is acceleration due to gravity. If the wavemaker frequency varies linearly from Ω_1 to Ω_2 ($\Omega_1 > \Omega_2$) following $\frac{d\Omega}{dt} = -\frac{g}{2x_f}$ within the time interval $[t_1, t_2]$, Longuet-Higgins (1974) showed that the energy of each wave packet emitted during this period will converge at $x = x_f$ simultaneously at $t = t_f$ (see Brown & Jensen (2001)). This focussing of wave energy thus causes a momentary but significant increase in energy density at x_f manifested as a transient, large amplitude wave at that location around time t_f . This technique has been discussed in Davis & Zarnick (1964) and its variants have been employed extensively to generate breaking waves in the laboratory in a predictable manner in two (Rapp & Melville 1990) and three dimensions (Wu & Nepf 2002; Johannessen & Swan 2001; McAllister *et al.* 2022) as well as in other related contexts such as generation of parasitic capillary on large amplitude waves (Xu & Perlin 2023).

On the other hand, in non-linear dispersive focusing, the modulational instability (Benjamin & Feir 1967) of a uniform, finite-amplitude wavetrain (Stokes wave) plays a crucial role. This instability can cause the wave train to split into groups, where focusing within a group can produce a wave significantly larger than the others (Zakharov *et al.* 2006). For further details on nonlinear focusing, we refer readers to the review by Onorato *et al.* (2013).

Spatio-temporal focussing at gravito-capillary scales

Following this brief introduction to large-scale focusing, we now focus on length scales where gravitational and capillary restoring forces are nearly equivalent. Our study aims to achieve an analytical understanding of wave focusing at these shorter scales. Below, we illustrate two examples where such small-scale focusing can be readily observed.

Stuhlman Jr (1932) investigated the formation of drops from collapsing bubbles with diameters under 0.12 cm in water-air interfaces and 0.15 cm in benzene-air interfaces. He hypothesised that these drops emerged from Worthington jets created by the collapse of the bubble cavity. However, contemporary research identifies this as just one of two mechanisms responsible for drop generation (Villermaux *et al.* 2022). The first high-speed (≈ 6000 frames per second) images of jet formation were reported by MacIntyre (1968, 1972) (see original experiments by Kientzler *et al.* (1954)). Interestingly, these studies demonstrated that the surface ripples are created by the retraction of the circular rim of the relaxing bubble

cavity. These ripples travel towards the cavity base before the jet emerges. In the words of [MacIntyre \(1972\)](#) (see abstract) “...an irrotational solitary capillary ripple precedes the main toroidal rim transporting mass along the surface at about 90% of its phase velocity. The convergence of this flow creates opposed jets...”. The seminal work by [Duchemin et al. \(2002\)](#) of collapsing bubbles (much smaller than their capillary length scale) at a gas-liquid interface was able to resolve this focussing process, via direct numerical simulations (DNS) of the axisymmetric Navier-Stokes equations without gravity. [Figure 1](#) depicts the generation of an axisymmetric, wave-train focussing towards the base of the bubble cavity (also the symmetry axis) for two different Ohnesorge numbers (Oh) and at a fixed Bond number (Bo). The Bond number $Bo \equiv \frac{\rho^L g \hat{R}_b^2}{T}$ determines the bubble shape, and Ohnesorge number $Oh \equiv \frac{\mu^L}{\sqrt{\rho^L T \hat{R}_b}}$ accounts for the ratio of viscous to capillary forces. Here ρ^L , μ^L , T , \hat{R}_b are the lower fluid density, lower fluid viscosity, coefficient of surface tension and equivalent radius of the bubble respectively. We refer the readers to [Deike \(2022\)](#); [Sanjay \(2022\)](#); [Gordillo & Blanco-Rodríguez \(2023\)](#) for recent advances on study of bubble collapse and jet formation mechanisms.

Another example of axisymmetric focussing of surface waves was highlighted in the study by [Longuet-Higgins \(1990\)](#), where several interesting observations were noted. [Longuet-Higgins \(1990\)](#) studied the inverted conical shaped ‘impact cavities’ seen in experiments and simulations ([Oguz & Prosperetti 1990](#)) of a liquid droplet falling on a liquid pool. The author compared these cavities to an exact solution to the potential flow equations without surface tension or gravity ([Longuet-Higgins 1983](#)), where the free-surface (gas-liquid interface) took the form of a cone at all time. The apex of this cone (i.e. the impact cavity) is often seen to contain a bulge (see fig. 2a in [Longuet-Higgins \(1990\)](#)) and the formation of this was attributed to (we quote, section 6 first paragraph in [Longuet-Higgins \(1990\)](#)) “a ripple on the surface of the cone converging towards the axis of symmetry”, thus highlighting the role of wave focussing once again. [Longuet-Higgins \(1990\)](#) insightfully remarked that this convergence process would be similar to the radially inward propagation of a circular ripple on a water surface. The interface shape could thus be approximated as being due to the linear superposition of an initial, localised wave packet (generated by distorting an initially flat surface) whose Fourier-Bessel representation $F(k)$ (k being the wavenumber) slowly varies on a time-scale \bar{t} (i.e. slow compared to the wave packet propagation time-scale t). [Longuet-Higgins \(1990\)](#) thus posits that the shape of the perturbed interface $\eta(r, t, \bar{t})$ may be represented as

$$\eta(r, t, \bar{t}) = \int_{\Delta k} F(k, \bar{t}) J_0(kr) \exp(I\sigma(k)t) k dk, \quad (1.1)$$

where J_0 is the Bessel function, r is the radial coordinate and the spectrum of the surface perturbation $F(k, \bar{t})$ evolves slowly on a time-scale \bar{t} , $I \equiv \sqrt{-1}$ and $\sigma(k)$ satisfies the dispersion relation for capillary waves (see eqn. 6.2 in [Longuet-Higgins \(1990\)](#)). Note that if the slow variation of $F(k, \bar{t})$ over \bar{t} is suppressed, eqn. 1.1 represents the solution to the linearised Cauchy-Poisson problem with an initial surface distortion whose Hankel transform is $F(k)$. [Longuet-Higgins \(1990\)](#) however did not report any systematic comparison of available experimental or simulational data ([Oguz & Prosperetti 1990](#)) with eqn. 1.1 although the author anticipated that nonlinearity could become important during the convergence; see last para in page 405 of [Longuet-Higgins \(1990\)](#).

Our current study is partly motivated by the aforementioned observations of [Longuet-Higgins \(1990\)](#) and [Duchemin et al. \(2002\)](#) and aims at obtaining an analytical description of spatio-temporal wave focussing at these short scales. We seek an initial, *localised* surface

distortion which produces a wave-train, and whose radial convergence may be studied analytically, at least in the potential flow limit. We refer the reader to the review by [Eggers *et al.* \(2024\)](#) where this limit corresponding to Ohnesorge $Oh = 0$ is discussed. In the next section we present a localised initial surface distortion which is expressible as a linear superposition of eigenmodes. It will be seen that this distortion generates a surface wave-train which focuses towards the symmetry axis of the container. We emphasize that the wave-trains or the solitary ripple seen in [Kientzler *et al.* \(1954\)](#) and [Longuet-Higgins \(1990\)](#) respectively, have different physical origins compared to the ones we study here. However, following [Longuet-Higgins \(1990\)](#) we intuitively expect there are aspects of their convergence which do not sensitively depend on how these are generated in the first place.

We further develop an inviscid nonlinear theory for the focusing of a concentric wave-train resulting from the aforementioned *a priori* imposed free-surface deformation. The theory developed from first principles here has no fitting parameters and helps delineate those aspects of focusing which may be accounted for by linear theory compared to nonlinear features. In a series of earlier theoretical and computational studies from our group ([Farsoiya *et al.* 2017](#); [Basak *et al.* 2021](#); [Kayal *et al.* 2022](#); [Kayal & Dasgupta 2023](#)), we have solved the initial-value problem corresponding to delocalised, initial interface distortions in the form of a single eigenmode ($J_0(kr)$) at gravity dominated large-scales ([Kayal & Dasgupta \(2023\)](#)), gravito-capillary intermediate scales ([Farsoiya *et al.* 2017](#); [Basak *et al.* 2021](#)) and capillarity dominated small-scales ([Kayal *et al.* \(2022\)](#)) (also see the recent study in [Dhote *et al.* \(2024\)](#) for a delocalised initial perturbation on a sessile bubble). In contrast to these studies, we study here a *localised, multimodal* initial excitation. Apart from the obvious advantage of easier experimental realisation of this initial condition (see [Ghabache *et al.* \(2014b\)](#) for experimental realisation at gravity dominated scales), this initial condition has the additional advantage that already at linear order, a radially propagating concentric wave-train is obtained and one can ask how does this converge at the axis of symmetry? In contrast, for a single mode initial condition as in [Basak *et al.* \(2021\)](#); [Kayal *et al.* \(2022\)](#), at linear order one obtains only a standing wave and it is necessary to proceed to quadratic order and beyond to generate other modes via non-linear interactions whose superposition can generate a focussing wave-train.

The manuscript is structured as follows: § 2 illustrates the time evolution of a relaxing cavity and introduces the analytical equations for wave evolution. § 3 compares these analytical results with direct numerical simulations (DNS). Finally, the paper culminates with discussions and outlook in § 4.

2. Time evolution of a relaxing cavity

As shown in fig. 2, the system consists of a cylindrical container of radius \hat{R} filled with quiescent liquid (indicated in blue). As we do not model the upper fluid in our theory, here onwards the superscript L is dropped from the variables representing fluid properties. For simplicity of analytical calculation, the cylinder is assumed to be infinitely deep and the gas-liquid density ratio is fixed at 0.001 to model air-water configuration. In our theoretical calculations, we approximate the gas-liquid interface as a free-surface and neglect any motion in the gas phase (although, it is modeled in our DNS). Some of the relevant length scales are the gravito-capillary length $l_c \equiv \sqrt{T/\rho g} \approx 2.7$ mm and the visco-capillary length scale $l_\mu \equiv \mu^2/\rho T \approx 0.01$ μm . For our chosen sizes of the initial interface perturbation (0.26 – 3.9 mm), these length scales justify the inclusion of both capillarity as well as gravity in the theoretical calculation while neglecting viscosity at the leading order. However, we stress that viscosity is known to have a non-monotonic effect on wave focussing in a collapsing bubble, as demonstrated by [Ghabache *et al.* \(2014a\)](#). Their fig. 3 shows that the jet velocity during

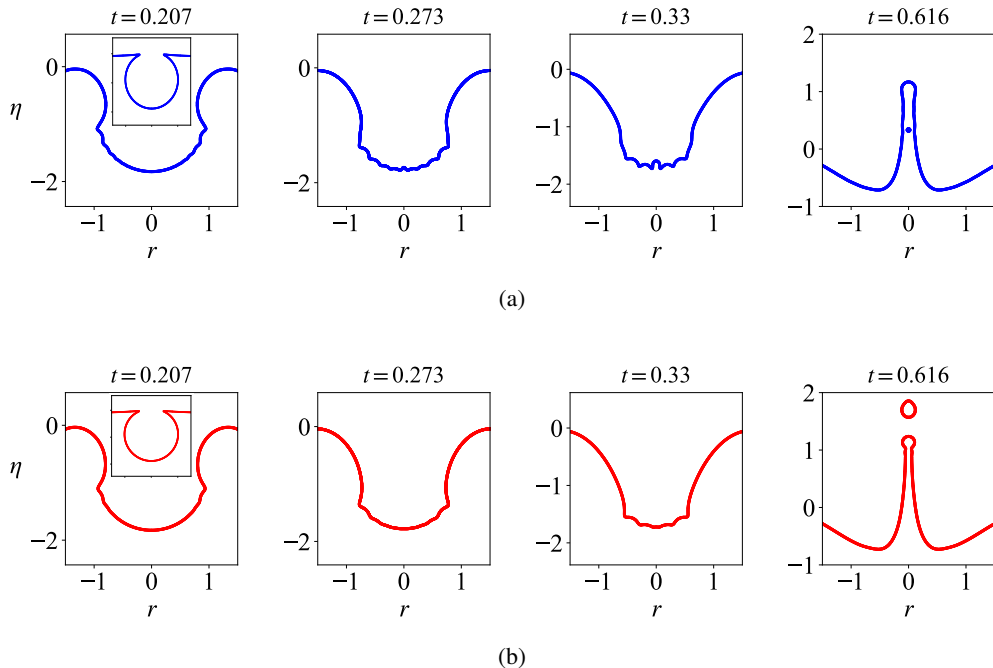


Figure 1: An example of capillary wave focussing obtained from direct numerical simulations (DNS) conducted using the open-source code Basilisk [Popinet & collaborators \(2013–2024\)](#). The initial cavity shape (inset in first figure of upper and lower panels) is obtained by solving the Young-Laplace equation with gravity to determine the shape of a static bubble at the free surface (without its cap). In CGS units, initial bubble radius 0.075, surface tension $T = 72$, gravity $g = 981$, density $\rho^L = 1.0$ and $\rho^U = 0.001$ for upper and lower fluid. Upper panel (blue) simulations are conducted using zero viscosity for both gas (above) and liquid (below). (Red, lower panel) simulations have dynamic viscosity $\mu^U = 0.0001$ and $\mu^L = 0.01$. Axes are non-dimensionalised using initial bubble radius. Time is non-dimensionalised using the capillary time-scale $t = \frac{\hat{t}}{\sqrt{\frac{\rho^L R_b^3}{T}}}$. For the upper panel $Bo \equiv \frac{\rho^L g R_b^2}{T} = 0.076$ and $Oh = \frac{\mu^L}{\sqrt{\rho^L T R_b}} = 0$. For the

lower panel $Bo = 0.076$ and $Oh = 0.0043$.

bubble bursting varies non-monotonically with increasing viscosity. Thus, the fastest jets occur not in an inviscid system but at an ‘optimal’ viscosity. In what follows, we employ potential flow equations in our theory and do not treat the boundary layers expected to be generated at the air-water interface and the cylinder walls ([Mei & Liu 1973](#)). We will address the inclusion of viscous effects later in the study.

Before delving into the theoretical formulation, it is instructive to discuss the phenomenology of the problem. Fig. 3, panels (a)-(i) depict the interface at various time instants as obtained from DNS. These are obtained by solving the inviscid, axisymmetric, and incompressible Euler’s equations with surface-tension and gravity in cylindrical coordinates (Basilisk, [Popinet & collaborators 2013–2024](#)) (script file is available as supplementary material ([Kayal 2024](#))). The images in fig. 3 are obtained by generating the surface of revolution of axisymmetric DNS data. As shown in panel (a), the interface is initially distorted in the shape of an axisymmetric, stationary, and *localised* perturbation. As this cavity relaxes, waves are generated which travel outward reflecting off the wall (between

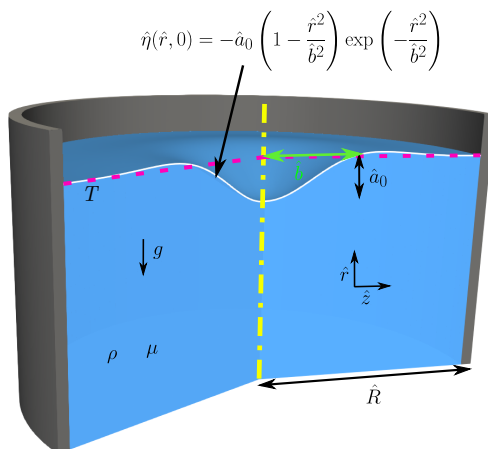


Figure 2: A (not to scale) cross-sectional representation of the initial interface distortion $\hat{\eta}(\hat{r}, 0)$ shaped as a cavity of half-width \hat{b} and depth \hat{a}_0 in a cylinder of radius \hat{R} filled with liquid (in blue). The functional form chosen for $\hat{\eta}(\hat{r}, 0)$ was first proposed by Miles (1968) and represents a volume preserving distortion. The red dotted line indicates the unperturbed level of the free-surface of the liquid pool. The gas-liquid surface tension is T . Liquid density and viscosity are ρ and μ respectively, g is gravity.

panels (e) and (f)). This produces a wave-train which focusses at the symmetry axis of the container ($r = 0$). One notes the formation of a small dimple-like structure at the symmetry axis in panel (h). In § 3, we will demonstrate that neither the dimple nor other interface features around the symmetry axis can be explained by the linear theory.

2.1. Governing equations: potential flow

We now turn to the theoretical analysis of the phenomenology illustrated in fig. 3. In the base state, we consider a quiescent pool of liquid with density ρ and surface tension T contained in a cylinder of radius \hat{R} . For analytical simplicity, we assume this pool is infinitely deep compared to the wavelength of the excited interface waves. For further simplicity, we assume that the solid-liquid contact angle at the cylinder wall is always fixed at $\pi/2$ and the contact line is free to move ($\partial_n v_t = 0$). This is the simplest contact line condition which allows for reflection of waves at the boundary without complicating the analytical treatment of the problem. The variables $\hat{\eta}(\hat{r}, \hat{t})$ are used to represent the axisymmetric perturbed interface (see fig. 1) and $\hat{\phi}(\hat{r}, \hat{z}, \hat{t})$ is the disturbance velocity potential; \hat{r} and \hat{z} being the radial and axial coordinates in cylindrical geometry respectively. Variables with the dimensions of length (e.g. \hat{r} , \hat{z} , $\hat{\eta}$) and time (\hat{t}) are scaled using length and time-scales $L \equiv \hat{R}$ and $T_0 \equiv \sqrt{\hat{R}/g}$, respectively. The velocity potential $\hat{\phi}$ is non-dimensionalised using the scale L^2/T_0 . Under the potential flow approximation, the nondimensional governing equations and boundary

conditions governing perturbed quantities are,

$$\frac{\partial^2 \phi}{\partial r^2} + \frac{1}{r} \frac{\partial \phi}{\partial r} + \frac{\partial^2 \phi}{\partial z^2} = 0, \quad (2.1a)$$

$$\frac{\partial \eta}{\partial t} + \left(\frac{\partial \eta}{\partial r} \right) \left(\frac{\partial \phi}{\partial r} \right)_{z=\eta} - \left(\frac{\partial \phi}{\partial z} \right)_{z=\eta} = 0, \quad (2.1b)$$

$$\left(\frac{\partial \phi}{\partial t} \right)_{z=\eta} + \eta + \frac{1}{2} \left\{ \left(\frac{\partial \phi}{\partial r} \right)^2 + \left(\frac{\partial \phi}{\partial z} \right)^2 \right\}_{z=\eta} - \alpha \left\{ \frac{\frac{\partial^2 \eta}{\partial r^2}}{\left\{ 1 + \left(\frac{\partial \eta}{\partial r} \right)^2 \right\}^{\frac{3}{2}}} + \frac{1}{r} \frac{\frac{\partial \eta}{\partial r}}{\left\{ 1 + \left(\frac{\partial \eta}{\partial r} \right)^2 \right\}^{\frac{1}{2}}} \right\} = 0, \quad (2.1c)$$

$$\int_0^1 r \eta(r, t) dr = 0, \quad \left(\frac{\partial \phi}{\partial r} \right)_{r=1} = 0, \quad (2.1d,e)$$

$$\lim_{z \rightarrow -\infty} \phi \rightarrow \text{finite} \quad (2.1f)$$

$$\eta(r, t = 0) = -\varepsilon \left(1 - \frac{r^2}{b^2} \right) \exp \left(-\frac{r^2}{b^2} \right) = \sum_{m=1}^N \eta_m(0) J_0(k_m r), \quad \frac{\partial \phi}{\partial n}(r, z = \eta(r, 0), t = 0) = 0, \quad (2.1g,h)$$

where $\varepsilon > 0$ and n in eqn. 2.1h is a distance coordinate measured normal to the free-surface at $t = 0$. The dimensionless parameters are defined as follows: $\alpha \equiv \frac{T}{\rho g \hat{R}^2}$, representing the inverse Bond number (based on the cylinder radius); $b \equiv \frac{\hat{b}}{\hat{R}}$ is the dimensionless measure of cavity width; and $\varepsilon \equiv \frac{\hat{a}_0}{\hat{R}}$ is the dimensionless measure of cavity depth (see Fig. 2 caption for the meaning of the symbols).

In cylindrical, axisymmetric coordinates, eqn. 2.1a is the Laplace equation, 2.1b and 2.1c are the kinematic boundary condition and the Bernoulli equation applied at the free surface respectively. Eqn. 2.1d restricts initial interfacial distortions to those which are volume conserving while 2.1e enforces no-penetration at the cylinder wall. Eqn. 2.1f is the finiteness condition at infinite depth.

Eqns. 2.1 g & h represent the initial conditions. We decompose the initial interface distortion i.e. $\eta(r, t = 0) = -\varepsilon \left(1 - \frac{r^2}{b^2} \right) \exp \left(-\frac{r^2}{b^2} \right)$ (Miles 1968), into a sum of Bessel modes as indicated by the second equality sign in eqn. 2.1g and $J_1(k_m) = 0$ for $m \in \mathbb{Z}^+$. The numerical values of the modal coefficients at $t = 0$ i.e. $\eta_m(0)$ ($m = 1, 2, 3 \dots$) in eqn. 2.1g are determined from the orthogonality relation between Bessel functions i.e.

$\eta_m(0) = \frac{\int_0^1 dr r J_0(k_m r) \eta(r, 0)}{\int_0^1 dr r J_0^2(k_m r)}$. A sample representation of the initial condition and its modal coefficients is presented in fig. 4a and 4b respectively where it is seen that about 17 modes are excited initially. Subject to these initial and boundary conditions presented in eqns. 2.1 a-h, we need to determine the modal amplitudes $\eta_m(t)$, $m = 1, 2, 3 \dots$ as a function of time and this is carried out next.

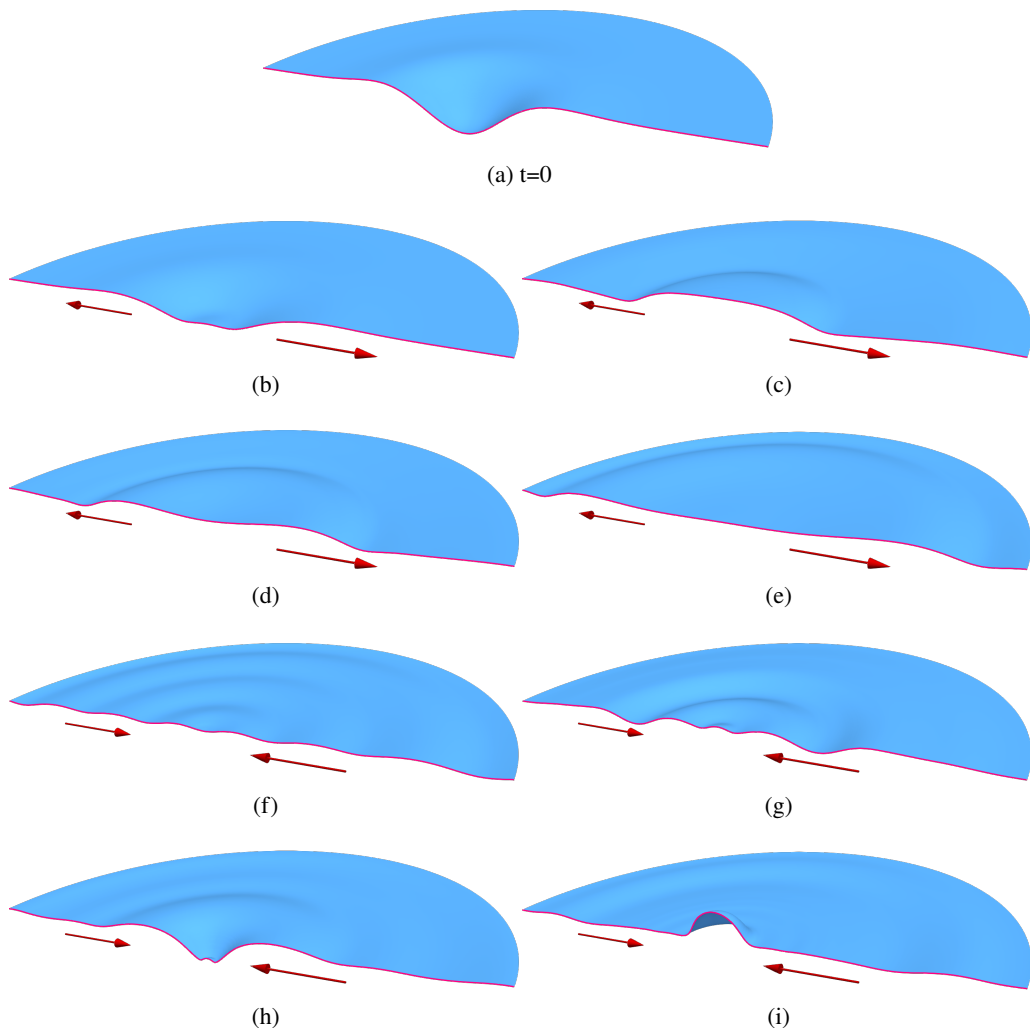


Figure 3: Wave focussing observed in DNS from the cavity-shaped interface distortion at $t = 0$ (panel (a)). The figure is to be read left to right and top to bottom for progression of time. After the waves reflect off the cylinder wall (between panels (e) and (f)); the confining walls are not shown), they focus inwards towards $r = 0$ producing strongly nonlinear oscillations of increasing amplitude. The arrows indicate the instantaneous direction of wave motion. The DNS parameters may be read from Case 1 in table 1.

2.2. Equations for modal amplitude $\eta_j(t)$

In this section we solve the initial, boundary-value problem posed in eqns. 2.2 a-h. We derive equations governing the time evolution of modal coefficients $\eta_j(t)$ upto quadratic order (i.e. terms which are cubic or higher in the modal coefficients are neglected). The approach for doing this is classical and was laid out in Hasselmann (1962) in Cartesian coordinates although their initial conditions were random functions in contrast to the deterministic initial distortion posed in eqn. 2.1g. The procedure below closely follows the approach of Nayfeh (1987), who derived similar equations (his eqns. 14 and 15) in the context of the Faraday instability (i.e. with vertical oscillatory forcing) including gravity but not surface tension (Nayfeh 1987) in his analysis. In contrast to forced waves being studied by Nayfeh (1987),

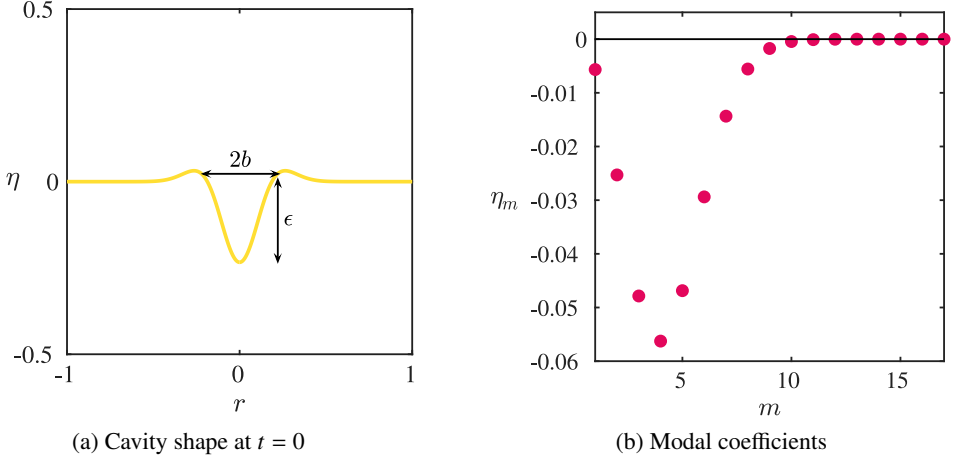


Figure 4: Panel (a) The gas-liquid interface initially deformed as a cavity of half-width $b = \frac{\hat{b}}{\hat{R}}$ and depth $\varepsilon \equiv \frac{\hat{a}_0}{\hat{R}}$. Panel (b) The modal coefficients $\eta_m(0)$ obtained by decomposing the initial distorted interface. For this initial distortion, $\varepsilon = 0.091$, $b = 0.187$. It is seen that only the first ten modes or so are excited initially. For accuracy, we consider the energy in the first seventeen modes initially ($m = 1, 2, 3 \dots 17$).

we consider free waves in our current study and include both surface-tension and gravity in the analysis. We first expand ϕ and η in eqns. 2.1 as

$$\phi(r, z, t) = \sum_{m=1}^{\infty} \phi_m(t) J_0(k_m r) \exp(k_m z), \quad \eta(r, t) = \sum_{m=1}^{\infty} \eta_m(t) J_0(k_m r) \quad (2.2a, b)$$

By construction, each term in the expansion in 2.2 satisfies the Laplace equation 1.1a, eqns. 2.1 (d) and (e) as well as the finiteness condition 2.1f. Taylor expanding eqns. 2.1b and c about $z = 0$ we obtain

$$\frac{\partial \eta}{\partial t} - \left(\frac{\partial \phi}{\partial z} \right)_{z=0} - \left(\frac{\partial^2 \phi}{\partial z^2} \right)_{z=0} \eta + \frac{\partial \eta}{\partial r} \left(\frac{\partial \phi}{\partial r} \right)_{z=0} + \text{H.O.T} = 0 \quad (2.3a)$$

$$\left(\frac{\partial \phi}{\partial t} \right)_{z=0} + \eta \left(\frac{\partial^2 \phi}{\partial t \partial z} \right)_{z=0} + \eta + \frac{1}{2} \left\{ \left(\frac{\partial \phi}{\partial r} \right)^2 + \left(\frac{\partial \phi}{\partial z} \right)^2 \right\}_{z=0} - \alpha \left\{ \frac{\frac{\partial^2 \eta}{\partial r^2}}{\left\{ 1 + \left(\frac{\partial \eta}{\partial r} \right)^2 \right\}^{\frac{3}{2}}} + \frac{1}{r} \frac{\frac{\partial \eta}{\partial r}}{\left\{ 1 + \left(\frac{\partial \eta}{\partial r} \right)^2 \right\}^{\frac{1}{2}}} \right\} + \text{H.O.T} = 0 \quad (2.3b)$$

where H.O.T represents higher order terms. Substituting expansions 2.2a & b into 2.3a,b and using orthogonality relations between Bessel functions we obtain for $n, p, m \in \mathbb{Z}^+$

$$\frac{d\eta_n}{dt} - k_n\phi_n(t) + \sum_{m,p} \left(D_{npm} - k_m^2 C_{npm} \right) \phi_m(t) \eta_p(t) = 0 \quad (2.4a)$$

$$\frac{d\phi_n}{dt} + (1 + \alpha k_n^2) \eta_n(t) + \sum_{m,p} k_m C_{npm} \left(\frac{d\phi_m}{dt} \right) \eta_p(t) + \frac{1}{2} \sum_{m,p} (D_{npm} + k_m k_p C_{npm}) \phi_m(t) \phi_p(t) = 0 \quad (2.4b)$$

$n = 1, 2, 3 \dots$

The nonlinear interaction coefficients C_{npm} and D_{npm} in eqn. 2.4 are related as (Nayfeh 1987):

$$D_{npm} = \frac{1}{2} \left(k_p^2 + k_m^2 - k_n^2 \right) C_{npm} \quad (2.5)$$

and $C_{npm} = \frac{\int_0^1 r J_0(k_n r) J_0(k_p r) J_0(k_m r) dr}{\int_0^1 r J_0^2(k_n r) dr}$. For the benefit of the reader, the detailed proof

of 2.5 is provided in Appendix A. Retaining self-consistently up to quadratic order terms, eqns. 2.4 a and b may be combined into a second order equation for η_n alone. This is:

$$\begin{aligned} & \frac{d^2\eta_n}{dt^2} + \omega_n^2 \eta_n + k_n \sum_{m,p} \left[2 + \frac{k_p^2 - k_m^2 - k_n^2}{2k_m k_n} \right] C_{npm} \left(\frac{d^2\eta_m}{dt^2} \right) \eta_p \\ & + \frac{1}{2} k_n \sum_{m,p} \left[1 + \frac{k_p^2 + k_m^2 - k_n^2}{2k_m k_p} + \frac{k_p^2 - k_m^2 - k_n^2}{k_m k_n} \right] C_{npm} \left(\frac{d\eta_m}{dt} \right) \left(\frac{d\eta_p}{dt} \right) = 0 \end{aligned} \quad (2.6)$$

Note that ω_n is the linear oscillation frequency of the n^{th} mode, viz. $\omega_n \equiv \sqrt{k_n (1 + \alpha k_n^2)}$. We solve the coupled ordinary differential eqns. 2.6 numerically subject to the initial conditions discussed earlier for $n = 1, 2, 3, \dots, 34$ (i.e. twice the initial number of excited modes, see fig. 4b) using ‘DifferentialEquations.jl’, an open-source package by Rackauckas *et al.* (2017) and collaborators. The ‘DifferentialEquations.jl’ automatically chooses an ODE solver based on stiffness detection algorithms as described by Rackauckas & Nie (2019). The Julia script file can be found in Kayal (2024). We note that while numerically solving eqn. 2.6, we compute $\frac{d^2\eta_m}{dt^2}$ in the third term of the equation (the nonlinear term) via the linear estimate, viz. $\frac{d^2\eta_m}{dt^2} = -\omega_m^2 \eta_m$. Interestingly, the solution to eqn. 2.6 shows instability at large times for sufficiently large modal amplitudes, in qualitative agreement with the stability analysis of Zhu *et al.* (2003) of axisymmetric standing waves (see their fig. 12). In further analysis, we restrict ourselves to numerical solutions to eqn. 2.6 which do not contain this instability within the time period of our interest in this study i.e. the time taken of focussing of the wave-train.

As benchmarking of our numerical solution procedure, we first solve eqns. 2.6 employing the single mode initial surface distortion that was studied in Basak *et al.* (2021) i.e. in our current notation $\eta(r, t = 0) = \varepsilon J_0(l_5 r)$, $\varepsilon > 0$ where $l_5 = 16.4706$ is the fifth non-trivial root of the Bessel function J_1 . For this initial condition, the second-order accurate solution is expectedly of the form

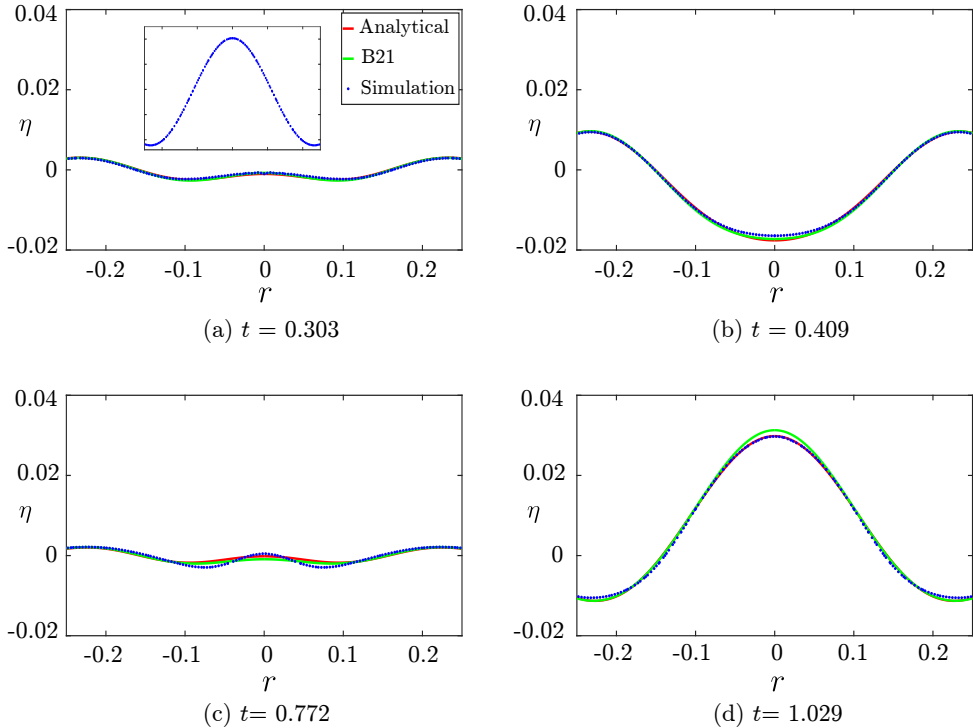


Figure 5: Benchmarking of our solution procedure for solving the coupled O.D.E.'s in eqns. 2.6 against inviscid DNS (indicated as ‘Simulation’ in the legend of panel (a)) and analytical predictions by Basak *et al.* (2021), indicated as ‘B21’. For DNS, the dimensionless parameters are $\varepsilon \equiv \frac{a_0}{\hat{R}} = \frac{0.5}{16.4706} = 0.03$, $\alpha = 0.004$ and $Oh = 0$. Note that the initial condition here has a crest around $r = 0$, see inset of panel (a).

$$\eta(r, t) = \varepsilon \eta_1(r, t) + \varepsilon^2 \eta_2(r, t) \quad (2.7)$$

where explicit expressions for η_1 and η_2 were provided in Basak *et al.* (2021) (we note the slight difference in non-dimensionalisation of length between the current study and the one by Basak *et al.* (2021) involving a factor of l_q). Fig. 5, demonstrates a comparison between the prediction of eqn. 2.7 (indicated in the figure as ‘B21’ for Basak *et al.* (2021)), the solution obtained from solving eqn. 2.6 with the same initial condition (labelled in the figure as ‘Analytical’) and the numerical simulation from Basilisk (depicted as ‘Simulation’). Fig. 5 demonstrates good agreement between the three, thereby providing confidence on our numerical procedure for solving eqns. 2.6.

3. Comparison of direct numerical simulations (DNS) with theory

In this section, we compare results from our direct numerical simulations with the theory discussed in § 2. Before this, it is instructive to rationalize the reflection process and estimate its duration. To do this, we observe that the Fourier-Bessel spectrum of the initial interface distortion prominently features a mode at $m = 4$ (see Fig. 4b). A rough estimate of the time required for the energy associated with any mode excited in the initial spectrum to complete a return trip (from $\hat{r} = 0$ to the wall and back) can be derived from linear theory.

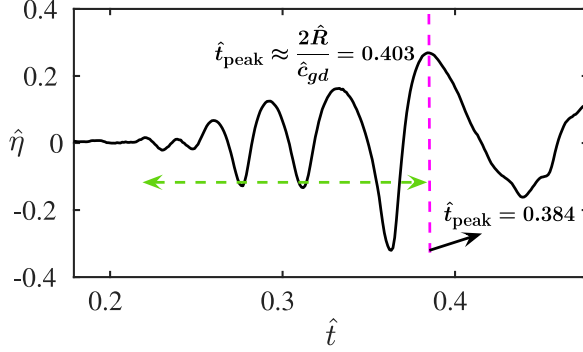


Figure 6: Time signal of the interface at $\hat{r} = 0$. The green line indicates approximately the time window when focussing takes place at $\hat{r} = 0$

When this return time is estimated for the dominant mode in the initial spectrum, we expect the numerical value to roughly coincide with the generation time of the largest amplitude oscillation at $\hat{r} = 0$ during the focusing process. This is illustrated in Fig. 6, where the time signal from tracking the interface at $\hat{r} = 0$ is presented (case 2 in Table 1). Note that this figure uses dimensional variables, denoted with hats. After the outward travelling waves move away, the interface at $\hat{r} = 0$ remains relatively quiescent, as indicated by the nearly flat time signal around $\hat{t} = 0.2$ s. As a result of reflection, the energy associated with every mode of wavenumber k present initially focusses back to $\hat{r} = 0$, this return trip is carried out with its group-velocity $\hat{c}_g = \frac{g+3(T/\rho)k^2}{2\sqrt{gk+Tk^3}/\rho}$. In fig. 4b, the dominant mode is $k_d = \frac{l_d}{R}$ and the largest oscillation at $\hat{r} = 0$ during the focussing process is seen to be generated at $\hat{t}_{\text{peak}} = 0.384$ s from fig. 6. Using the linear estimate $\hat{t}_{\text{peak}} \approx \frac{2\hat{R}}{\hat{c}_{gd}}$ where \hat{c}_{gd} is the group-velocity of the dominant mode, we obtain the value 0.403 s which is reasonably close to the observed $\hat{t}_{\text{peak}} = 0.384$ s.

In the collage of images in figs. 7 and 8, we present the shape of the interface as a function of time for case 1 and 2 in table 1 respectively, comparing this to linear and nonlinear theoretical predictions. The only difference between these two figures is in the value of ε , all other dimensionless numbers remaining the same. Here linear theory implies solution to eqn. 2.6 without the nonlinear terms. Note that this is equivalent to superposition of the form $\eta(r, t) = \sum_{m=1}^{17} J_0(k_m r) \cos(\omega_m t)$ where $\omega_m(k_m)$ satisfies the gravito-capillary dispersion relation for deep water. In fig. 7, the transition from outward propagating waves to inward propagating ones occur between panels (c) and (d). For panels (a), (b) and (c) it is evident that linear theory represents the outgoing waves accurately. However as focussing commences from panel (d) onwards, we notice significant differences between linear theory and (inviscid) DNS. Interestingly, second order theory seems to predict the shape of the interface around $r = 0$ quite well. Fig. 8 shows a more intense scenario than Fig. 7, featuring a larger $\varepsilon = 0.091$. The transition from predominantly linear to nonlinear behavior occurs between panels (c) and (d), representing outgoing and incoming waves, respectively. Notably, sharp dimple-like structures emerge around $r = 0$, as seen in panel (h), which are well described by nonlinear theory. Additionally, the tendency to form jets, as seen in the final panel, is noteworthy, although the nonlinear theory is only qualitatively accurate in this context. We refer the reader to the accompanying Movie #1 ($\varepsilon = 0.061$) and #2 ($\varepsilon = 0.091$), see additional supplementary material which visualises these.

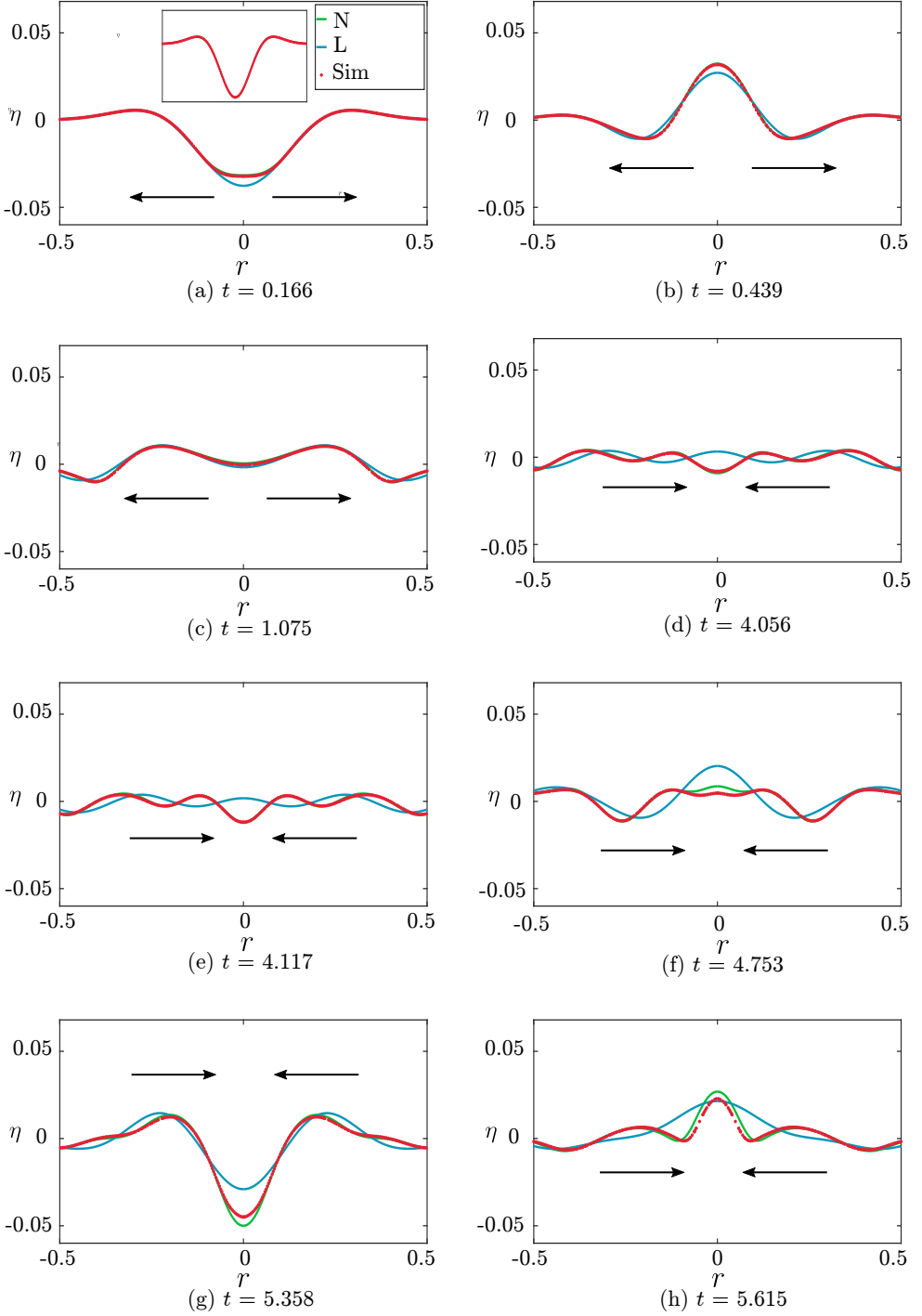


Figure 7: Waves generated from the cavity shaped interface distortion at $t = 0$ (inset of panel (a)). We compare the interface shape as a function of time as predicted by linear theory (L, solid blue line), second-order nonlinear theory (N, solid green line) and (inviscid) DNS (Sim, red symbols). The waves reflect-off the cylinder wall at $r = 1$ (not shown) and focus back towards $r = 0$ generating oscillations of increasing amplitude. This corresponds to case 1 of table 1 with $\varepsilon = 0.061$. To highlight the difference between linear and nonlinear predictions, the figures have been plotted upto $r = 0.5$ instead of the entire radial domain up to $r = 1$. The arrows depict the instantaneous direction of motion of the waves.

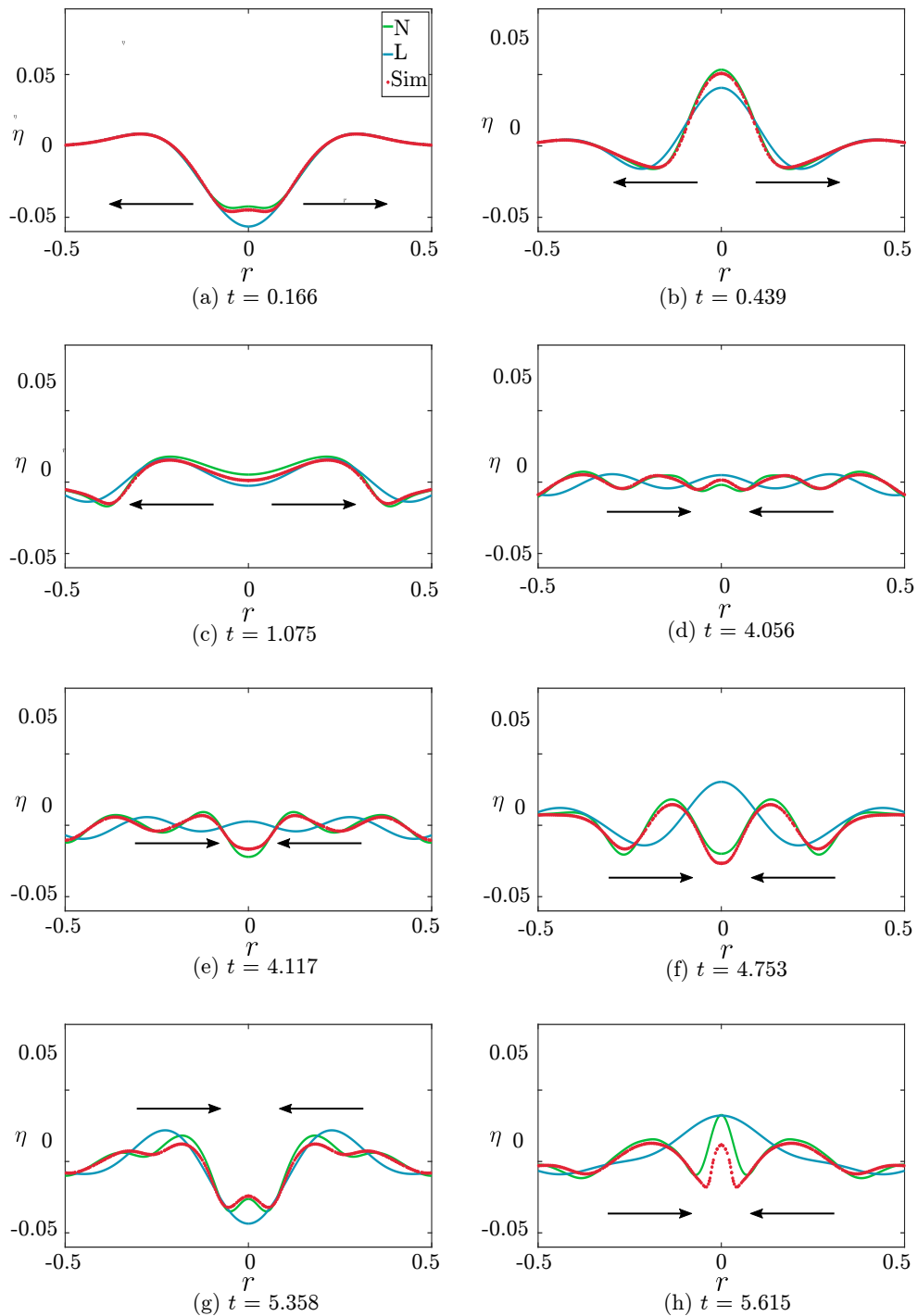


Figure 8: The same as fig. 7, but for $\varepsilon = 0.091$ corresponding to case 2 in table 1. Note the good qualitative agreement between nonlinear theory and (inviscid) DNS but not linear theory, in capturing the dimple in panel (g). Also note the large amplitude oscillations at $r = 0$ with a tendency to generate narrow jet-like structure (panel (h)).

Case	$\varepsilon \equiv \frac{\hat{a}_0}{\hat{R}}$	$Oh \equiv \frac{\mu}{\sqrt{\rho T \hat{b}}}$	\hat{a}_0	ν
1	0.061	0	0.26	0
2	0.091	0	0.39	0
3	0.091	1.17×10^{-5}	0.39	8.9×10^{-5}
4	0.091	1.17×10^{-4}	0.39	8.9×10^{-4}
5	0.091	1.17×10^{-3}	0.39	8.9×10^{-3}
6	0.091	1.17×10^{-2}	0.39	8.9×10^{-2}
7	0.006	0	0.026	0
8	0.006	1.17×10^{-5}	0.026	8.9×10^{-5}
9	0.006	1.17×10^{-4}	0.026	8.9×10^{-4}
10	0.006	1.17×10^{-3}	0.026	8.9×10^{-3}
11	0.006	3.7×10^{-3}	0.026	2.81×10^{-2}
12	0.006	1.17×10^{-2}	0.026	8.9×10^{-2}

Table 1: All dimensional lengths are indicated with a hat. Values are quoted in CGS units.

In all of the cases we have used $\hat{R} = 4.282$ cm, $\hat{b} = 0.8$ cm, $T = 72$ dyne/cm, $g = -981$

cm/s², $\rho = 1$ gm/cm³. These imply dimensionless values $b \equiv \frac{\hat{b}}{\hat{R}} = 0.187$,

$$\alpha \equiv \frac{T}{\rho g \hat{R}^2} = 0.004$$

3.1. Role of nonlinearity at $r = 0$

Figs. 7 and 8 show that although the linear solution is a reasonable model for the interface evolution before reflection, it shows deviation from the fully nonlinear simulation at the axis of symmetry during radial convergence of the wave-train. In this subsection, we explain the apparent significance of nonlinearity around the symmetry axis. To do this, we revisit results for the single-mode interface distortion described by $\eta(r, 0) = \varepsilon J_0(k_5 r)$ (where $\varepsilon > 0$ corresponds to an initial crest at $r = 0$ and $q = 5$ is the primary mode), as studied in Basak *et al.* (2021). For this initial condition, the expression for $\eta(r, t)$ was analytically derived up to $\mathcal{O}(\varepsilon^2)$ in Basak *et al.* (2021) as:

$$\eta(r, t) = \underbrace{\varepsilon J_0(k_5 r) \cos(\omega_5 t)}_{\text{Primary mode}} + \varepsilon^2 \sum_{j=1}^{\infty} \left[\underbrace{\zeta_1^{(j)} \cos(\omega_j t)}_{\text{Free modes}} + \overbrace{\zeta_2^{(j)} \cos(2\omega_5 t) + \zeta_3^{(j)}}^{\text{Bound modes}} \right] J_0(k_j r), \quad (3.1)$$

where $\zeta_1^{(j)} + \zeta_2^{(j)} + \zeta_3^{(j)} = 0, \forall j \in \mathbb{Z}^+$ to ensure that the initial condition is satisfied. Note that that expression 3.1 has been suitably modified from Basak *et al.* (2021) to make this compatible with the length and time scales in the present analysis. Here $\varepsilon = \frac{\hat{a}_0}{\hat{R}}$, frequency $\omega_j = \sqrt{k_j(1 + \alpha k_j^2)}$ and expressions for $\zeta_1^{(j)}$, $\zeta_2^{(j)}$ and $\zeta_3^{(j)}$ are provided in the Appendix of (Basak *et al.* 2021). As highlighted in eqn. 3.1, the expression for $\eta(r, t)$ comprises of three qualitatively different parts. The first term on the right hand side of eqn. 3.1 represents the primary mode which is excited at $t = 0$. This mode has wavenumber k_5 and oscillates harmonically with frequency ω_5 . Self interaction of the primary mode generates other modes; the so-called ‘‘free modes’’ in eqn. 3.1 arise at $\mathcal{O}(\varepsilon^2)$ and their temporal frequency satisfy the dispersion relation i.e. modes with wavenumber k_j have frequency ω_j . The third kind

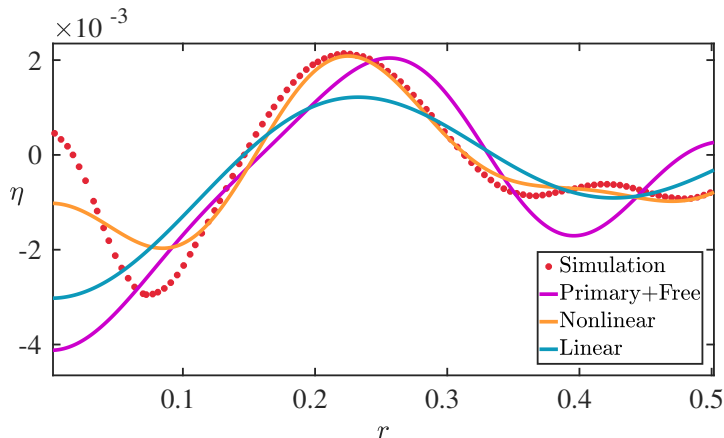


Figure 9: Various approximations for describing the dimple produced from a single mode initial perturbation

viz. the “bound modes” which too appear at $\mathcal{O}(\varepsilon^2)$ vary temporally with the frequency $2\omega_5$ (i.e. $\omega_5 + \omega_5$) or 0 (i.e. $\omega_5 - \omega_5$) independent of their wavenumber k_j .

In Fig. 9, the interface from inviscid DNS with the initial condition $\eta(r, 0) = \varepsilon J_0(k_5 r)$, $\varepsilon = 0.03 > 0$ is shown at an instant when it forms a dimple-like protrusion at $r = 0$. This is represented by the curve with red dots, labelled as ‘Simulation’. In this figure, we also plot the formula from Basak *et al.* (2021), excluding the bound components (labelled as ‘Primary + Free’), i.e., setting $\zeta_2^{(j)} = \zeta_3^{(j)} = 0$ in equation (3.1). It is evident that this approximation does not capture the dimple, which is otherwise predicted by the full nonlinear expression (indicated as ‘Nonlinear’ in the figure caption and referring to eqn. 3.1).

The above exercise can also be carried out when the initial interface deformation takes the shape of a cavity. For this initial condition, $\eta(r, 0) = \sum_{n=1}^{\infty} \eta_n(t) J_0(k_n r)$, as previously shown in fig. 4. From the numerical solution to eqns. 2.6, the temporal frequency spectrum at $r = 0$ is obtained. We track the time series generated by $\eta_n(t)$ and eliminate the frequencies $2\omega_n$ and 0 from its Fourier spectrum, thus removing the bound wave components for all initially excited modes. Fig. 10 demonstrates that after the removal of these bound modes, the interface (labeled ‘Primary + Free’) fails to capture the dimple shape. In contrast, the full numerical solution to eqns. 2.6 faithfully reproduces the dimple.

3.2. Viscous effects: comparison with linear theory

In this section, we analyze viscous effects for the chosen initial condition. Using cylindrical coordinates, Miles (1968) solved the problem of free-surface waves on a viscous liquid in a linear regime within a radially unbounded domain for multi-modal initial excitation. Farsoiya *et al.* (2017) extended this theory to internal waves, considering viscosity and density due to both upper and lower fluids, focusing on a single-mode initial perturbation. Due to the availability of superposition in the linear regime, the results of Farsoiya *et al.* (2017) are easily extended to multi-modal initial excitations as well. In Cartesian geometry, the single mode initial excitation case was first explicitly studied by Prosperetti (1976) treating free-surface waves and by Prosperetti (1981) treating internal waves. In the Laplace domain and in cylindrical axisymmetric coordinates, the solution to the evolution of a single mode was shown in Farsoiya *et al.* (2017) to be given by,

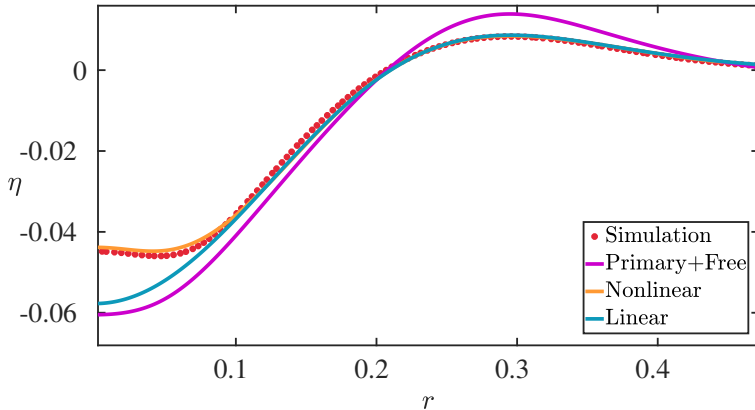


Figure 10: Shape of a dimple for a cavity with $\epsilon = 0.091$

$$\tilde{\eta}_m(s) = \hat{\eta}_m(0) \frac{s + \left(4\tilde{k}_m^2 \nu - \frac{4\tilde{k}_m^3 \nu}{\tilde{k}_m + \sqrt{\tilde{k}_m^2 + s/\nu}} \right)}{s^2 + \left(4\tilde{k}_m^2 \nu - \frac{4\tilde{k}_m^3 \nu}{\tilde{k}_m + \sqrt{\tilde{k}_m^2 + s/\nu}} \right) s + \hat{\omega}_m^2}, \quad \hat{\omega}_m^2 \equiv g\tilde{k}_m + T\tilde{k}_m^3/\rho, \quad \tilde{k}_m \equiv \frac{k_m}{\hat{R}} \quad (3.2)$$

Employing linear superposition, the corresponding (dimensional) expression for the interface evolution in the time domain for the current multi-modal case is

$$\hat{\eta}(\hat{r}, \hat{t}) = \sum_{m=1}^{17} \hat{\eta}_m(\hat{t}) J_0 \left(k_m \frac{\hat{r}}{\hat{R}} \right), \quad \hat{\eta}_m(\hat{t}) \equiv \mathcal{L}^{-1} [\tilde{\eta}_m(s)] \quad (3.3)$$

Here \mathcal{L}^{-1} is the inverse Laplace operator. We stress that expression 3.2 accounts for dissipation in the bulk liquid and boundary layer, as demonstrated by Prosperetti (1976) in Cartesian coordinates and by Farsoiyya *et al.* (2017) in cylindrical coordinates. Equation 3.3 is compared with DNS for two different values of ϵ and Oh in figs. 11 and 12, where inverse Laplace transforms were performed using the Cohen method by Henri Cohen & Zagier (2000) which is a default method in `mpmath` (2023), a free Python library for arbitrary-precision floating-point arithmetic. See Kayal (2024) for the code. Fig. 11 benchmarks the theory at a relatively small $\epsilon = 0.006$, where linear viscous theory is expected to be accurate. Excellent agreement with linear viscous theory is observed in Fig. 11. Conversely, fig. 12 shows a clear distinction between linear and nonlinear predictions.

To further investigate the impact of viscosity, fig. 13 presents the interfacial velocity at $r = 0$ from DNS for various Oh values. The most notable observation is that the highest peak velocity during wave focusing occurs in the *viscous* simulation rather than the inviscid one. This non-monotonous behavior as a function of the Ohnesorge number is a well-known phenomenon in other contexts (Ghabache *et al.* 2014a), indicating a significant effect of viscosity. In our analysis of converging waves, we attribute the observed non-monotonic behavior to viscous dissipation within the boundary layer at the gas-liquid interface. Even as the Ohnesorge number approaches zero ($Oh = 0^+$), this boundary layer remains significant, similar to the dissipative anomaly seen in fully developed turbulence (Prandtl 1904; Onsager 1949; Dubrulle 2019; Eggers 2018) and recently explored in contexts such as sheet retraction

(Sanjay *et al.* 2022) and drop impact (Sanjay *et al.* 2023) interfacial flows. Consequently, this non-zero viscous dissipation intensifies the focusing of capillary waves, thereby increasing the velocity at the center ($r = 0$). To validate this hypothesis, in the next section, we next employ the viscous potential flow approach, which accounts for bulk viscous dissipation but neglects dissipation in the gas-liquid boundary layer, to model the converging waves.

3.3. Viscous potential flow

To further elucidate viscous effects, we incorporate viscosity into the nonlinear equations using the viscous potential flow model (Joseph 2006). Unlike the linear case discussed previously, this method does not account for the boundary layer formed at the free surface, since it does not enforce the zero shear stress boundary condition (Moore 1963). As is well-known, in this approach the normal stress boundary condition (eqn. 2.1 c) is modified to incorporate the effect of bulk viscous damping to obtain

$$\begin{aligned} & \left(\frac{\partial \phi}{\partial t} \right)_{z=\eta} + \eta + 2 b Oh \sqrt{\alpha} \left(\frac{\partial^2 \phi}{\partial z^2} \right)_{z=\eta} + \frac{1}{2} \left\{ \left(\frac{\partial \phi}{\partial r} \right)^2 + \left(\frac{\partial \phi}{\partial z} \right)^2 \right\}_{z=\eta} \\ & - \alpha \left\{ \frac{\frac{\partial^2 \eta}{\partial r^2}}{\left\{ 1 + \left(\frac{\partial \eta}{\partial r} \right)^2 \right\}^{\frac{3}{2}}} + \frac{1}{r} \frac{\frac{\partial \eta}{\partial r}}{\left\{ 1 + \left(\frac{\partial \eta}{\partial r} \right)^2 \right\}^{\frac{1}{2}}} \right\} = 0. \end{aligned} \quad (3.4)$$

We follow the same strategy as the inviscid case and obtain a modified differential equation for η_n , i.e. the viscous counterpart of eqn. 2.6 leading to

$$\begin{aligned} & \frac{d^2 \eta_n}{dt^2} + \omega_n^2 \eta_n + 2 b Oh \sqrt{\alpha} k_n^2 \frac{d\eta_n}{dt} + 2b Oh \sqrt{\alpha} k_n \sum_{m,p} k_m^2 C_{npm} \frac{d\eta_m}{dt} \eta_p \\ & + k_n \sum_{m,p} \left[2 + \frac{k_p^2 - k_m^2 - k_n^2}{2k_m k_n} \right] C_{npm} \left(\frac{d^2 \eta_m}{dt^2} \right) \eta_p \\ & + \frac{1}{2} k_n \sum_{m,p} \left[1 + \frac{k_p^2 + k_m^2 - k_n^2}{2k_m k_p} + \frac{k_p^2 - k_m^2 - k_n^2}{k_m k_n} \right] C_{npm} \left(\frac{d\eta_m}{dt} \right) \left(\frac{d\eta_p}{dt} \right) = 0 \end{aligned} \quad (3.5)$$

In fig. 14, we compare the nonlinear analytical inviscid solution (referred to as ‘Inviscid’ in the legend), the viscous potential flow (VPF) solution for $\varepsilon = 0.091$ and the viscous DNS (referred to as ‘Simulation’) for Case 4 in table 1. It is seen that the VPF solution, is indistinguishable from the inviscid one in the limit of $Oh = 0^+$, highlighting the importance of resolving the viscous boundary layer in theory.

To further quantify the comparison between these cases, in fig. 15a shows the velocity at the axis of symmetry within a shallow cavity during focusing. The linear viscous theory, which accounts for the boundary layer at the free surface, describes the change in v_z with Ohnesorge number slightly better than the VPF model. Fig. 15b presents results for a deeper cavity where non-linearity plays a significant role, and the non-monotonic behavior observed in fig. 13 as a function of Oh is evident. The VPF model fails to capture this non-monotonic behavior, highlighting the importance of resolving the boundary layer at the gas-liquid interface, as discussed in § 3.2. We propose developing a nonlinear-viscous theory superior to the VPF model to explain the observations in Fig. 13 and Fig. 15b.

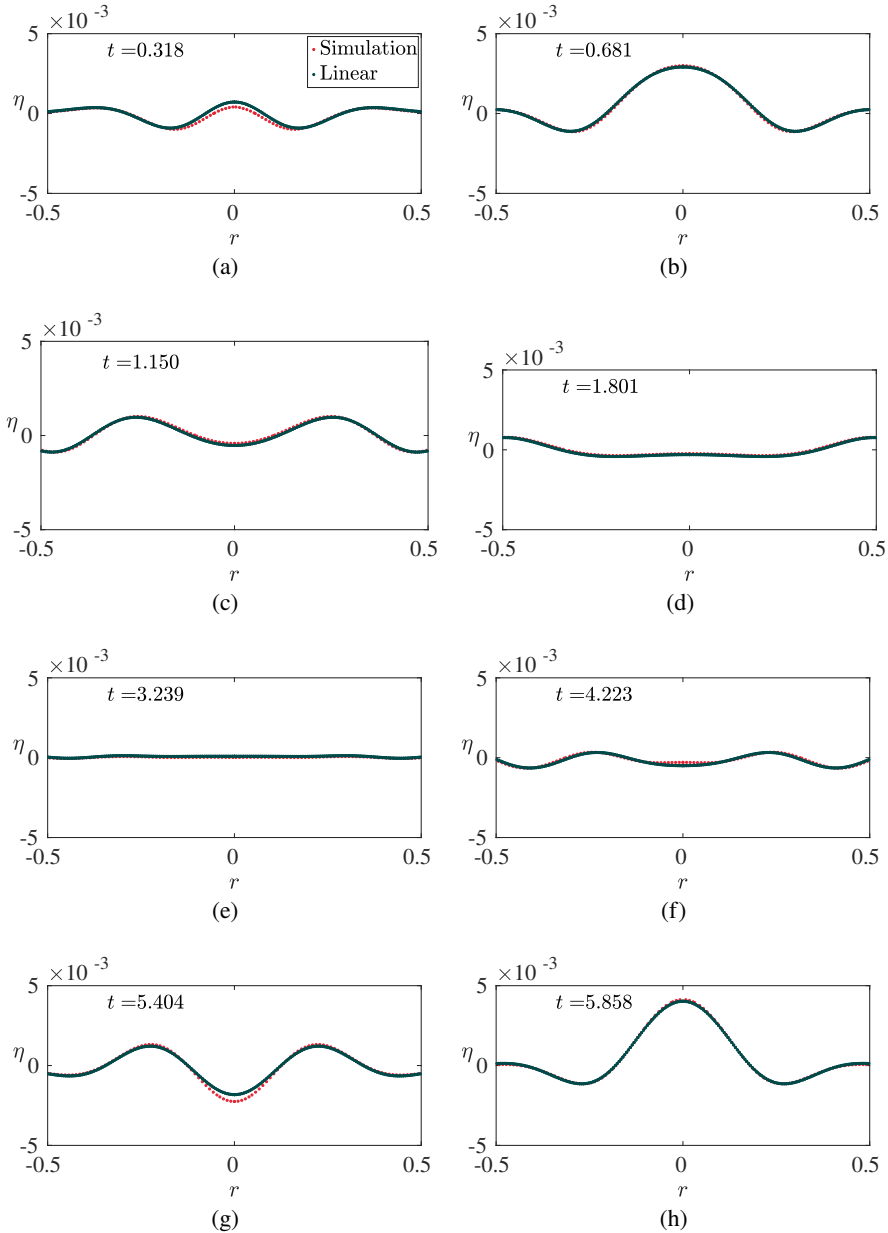


Figure 11: Viscous DNS (indicated as ‘Simulation’ with red dots in the legend to panel (a)) with $\varepsilon = 0.006$ and $Oh = 1.17 \times 10^{-3}$ corresponding to case 10 in table 1. One notes the excellent agreement with linear, viscous theory (green dots, ‘Linear’, eqn. 3.3 in text) with hardly any nonlinear contribution.

4. Conclusion & outlook

In this study, we have discussed the dynamics of a localised free-surface perturbation in a cylindrical pool of liquid, which generates a train of waves. These waves, upon reflecting from the container walls, converge back towards the axis of symmetry, leading to progressively increasing free-surface oscillations at the center. Using the potential flow approximation, we

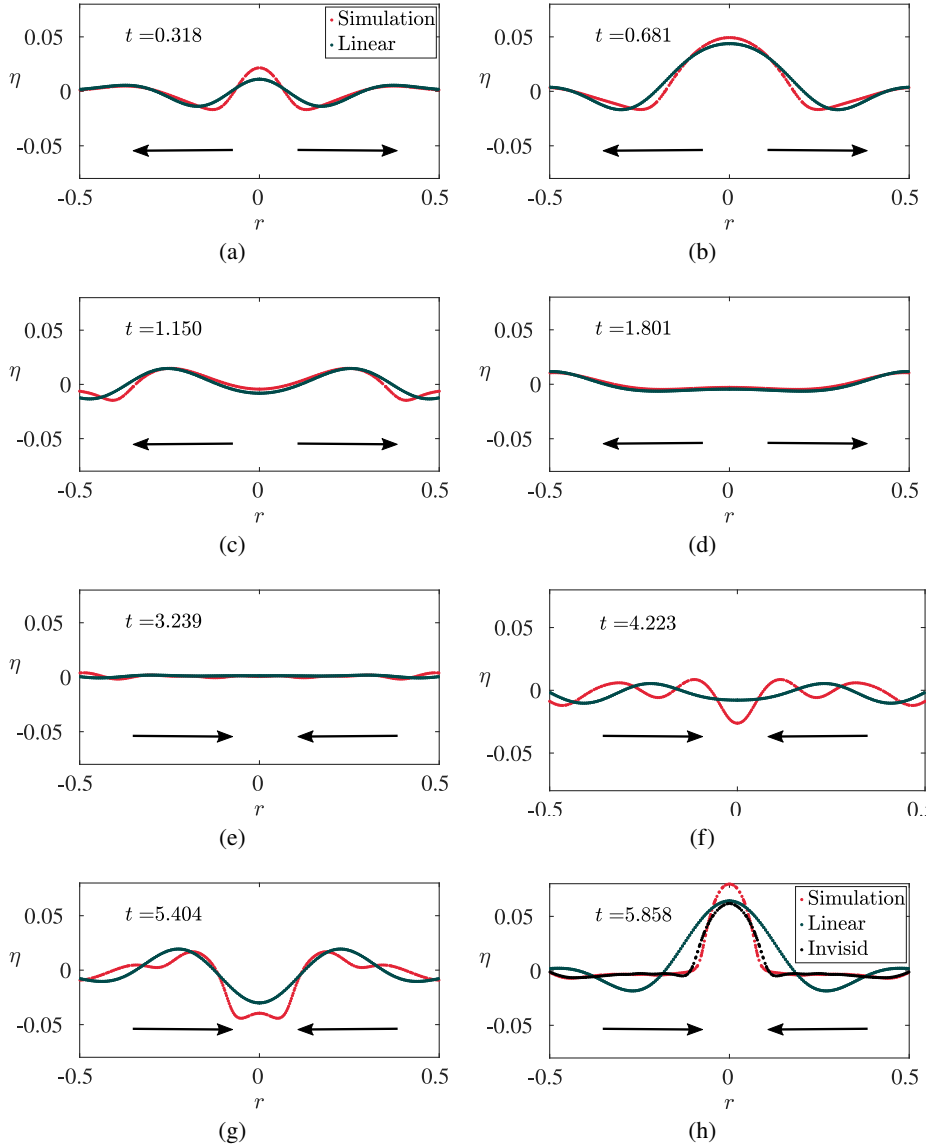


Figure 12: Viscous DNS (indicated as ‘Simulation’ with red dots in the legend to panel (a)) with $\varepsilon = 0.091$ and $Oh = 1.17 \times 10^{-4}$ corresponding to case 4 in table 1. In contrast to fig. 11, increasing the value of ε and a corresponding reduction in viscosity, has a dramatic effect in the simulations. We note that viscous linear theory is no longer adequate particularly during the focussing process in panels (f)-(h). In panel (h), we also provide a comparison of the interface at this time-instant, for the inviscid numerical simulation ($Oh = 0$) with the same ε . It is seen that the viscous simulation has a crest which at this instant is taller than the one obtained from the inviscid simulation.

derived a set of ordinary differential equations governing the evolution of modal amplitudes up to second order in the amplitude.

For shallow cavities, linear theory suffices to explain the wave evolution. However, as the cavity depth increases, the limitations of linear theory become evident, particularly in

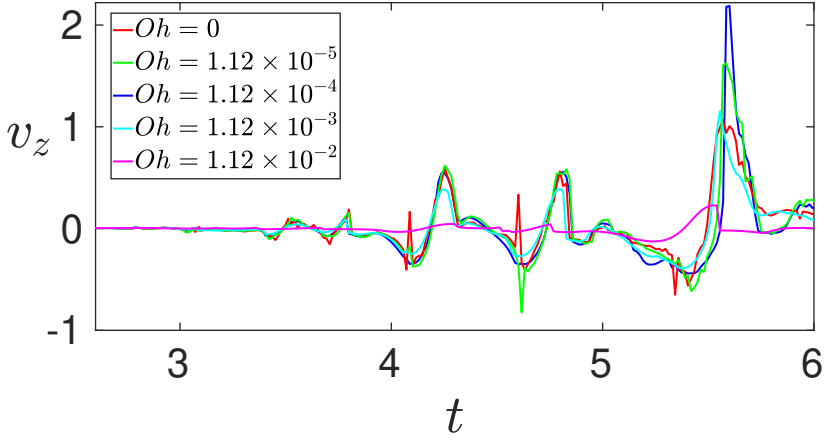


Figure 13: Velocity at the interface at $\hat{r} = 0$ for different values of Oh and fixed $\varepsilon = 0.091$.

Note that the viscous DNS for $Oh = 1.17 \times 10^{-4}$ (solid blue line) produces the largest velocity peak around $t \approx 5.7$. Note in particular that the inviscid signal ($Oh = 0$, red solid line) has a peak which is shorter by a factor of half compared to the signal corresponding to $Oh = 1.17 \times 10^{-4}$. We refer the reader to Appendix B where the grid convergence for this (and other) simulations are provided

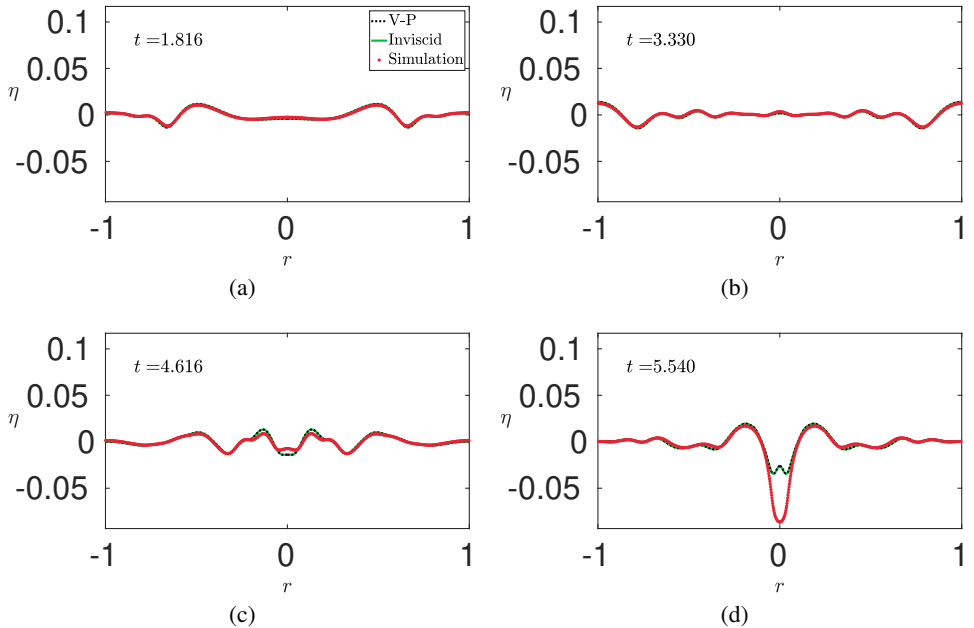


Figure 14: Comparison of the viscous potential solution (VPF, black dotted line), inviscid solution (green solid line) and DNS (red dots) at $\varepsilon = 0.091$ and $Oh = 1.17 \times 10^{-4}$, case 4 in table 1.

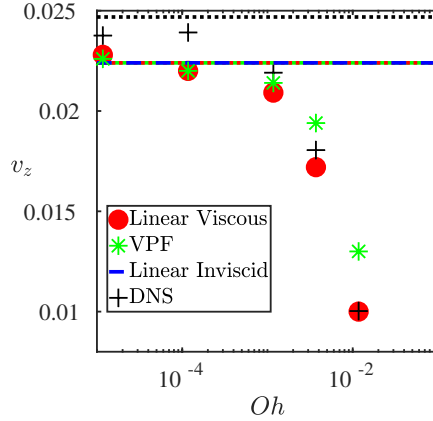
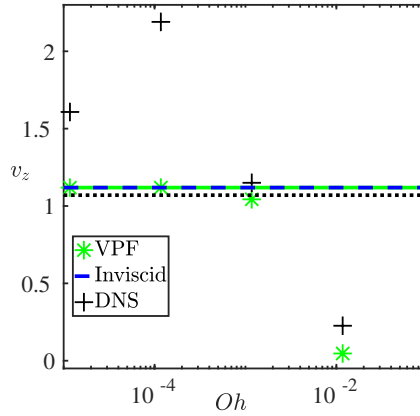
(a) Shallow cavity with $\varepsilon = 0.006$ (b) Deep cavity with $\varepsilon = 0.091$

Figure 15: Comparison of the maximum velocity at $r = 0$ after reflection for different Ohnesorge number for a shallow cavity, cases 7 – 12 in table 1 (panel a) and for a deep cavity, case 2 – 5 (panel b). Panel (a): ‘+’ symbols represent DNS with finite viscosity. Black dotted symbols represent DNS with zero viscosity. Red symbols represent the linear viscous solution obtained by numerical inversion of eqn. 3.2. Green symbols indicate viscous potential flow (VPF) approximation obtained from solving eqn. 3.5. At the $Oh = 0$ limit, VPF (green dashed line) and linear viscous theory (red dashed line) coincide with the linear inviscid theory (blue dashed line). Panel (b): Symbols have the same meaning as panel (a), the only difference is that we have employed nonlinear inviscid theory in this case. Note that non-monotonicity in the velocity at $r = 0$ as a function of Oh . The viscous potential flow approximation (VPF) despite being nonlinear is unable to describe this non-monotonicity, presumably because of its inability to resolve the boundary layer at the free-surface. In both of the panels, the dotted black line represents the velocity of inviscid DNS.

predicting the focusing effects at $r = 0$. Our findings demonstrate that linear dispersive focusing alone is inadequate to describe the intricate dimple shape forming at the axis of symmetry for deeper cavities. A nonlinear theory that accounts for energy transfer among various modes is essential for accurately modeling the cavity shape evolution. The role of bound modes is critical in capturing the emergence of the dimple.

A notable observation is the significant influence of viscosity on the focusing process. Contrary to expectations, the maximum velocity at the axis of symmetry is higher for a slightly viscous fluid than for an inviscid one. This non-monotonic behavior with respect to the Ohnesorge number Oh is not captured by either the linear viscous model (Farsoiyya *et al.* 2017; Prosperetti 1976) or the nonlinear viscous potential flow (VPF) model (Joseph 2006). The failure of the VPF model, which neglects the boundary layer effects, underscores the necessity of accounting for the boundary layer in the limit of $Oh \rightarrow 0^+$. The VPF model's convergence to an inviscid solution in this limit further strengthens the assertion that boundary layers are crucial for the observed velocity enhancements.

Future research should develop a comprehensive nonlinear viscous theory that incorporates both boundary layer effects and the nonlinearity of wave focusing. This theory would provide a more accurate analytical resolution of discrepancies observed in current models. Additionally, extending this work to non-Newtonian fluids, such as viscoplastic or viscoelastic liquids (Sanjay *et al.* 2021), could reveal new insights and broaden the applicability of our theoretical framework.

Acknowledgements. RD thanks Prof. B. Sutherland for sharing the study by Smith (1976).

Funding. We gratefully acknowledge financial support from DST-SERB (Govt. of India) grants MTR/2019/001240, CRG/2020/003707 and SPR/2021/000536 on topics related to waves, jet formation, cavity collapse and the viscous Cauchy-Poisson problem. The Ph.D. tenure of L.K. is supported by the Prime-Minister's Research Fellowship (PMRF), Govt. of India and is gratefully acknowledged.

Declaration of Interests. The authors report no conflict of interest.

Appendix A

We derive the relation between the nonlinear interaction coefficients C_{mnq} and D_{mnq} discussed in eqn. 2.5. This relation has been provided in Nayfeh (1987) and Miles (1976) without proof and the same is presented here. Following Nayfeh (1987), we represent eqn. 2.2 a in (semi) basis-independent notation as

$$\phi(\mathbf{x}, z, t) = \sum_{m=1}^{\infty} \phi_m(t) \Psi_m(\mathbf{x}) \exp(k_m z) \quad (4.1)$$

where \mathbf{x} is the horizontal position vector and Ψ_m satisfies the equation $\nabla_H^2 \Psi_m + k_m^2 \Psi_m = 0$ as a consequence of ϕ satisfying the Laplace eqn; note that $\nabla^2 = \nabla_H^2 + \frac{\partial^2}{\partial z^2}$. We assume that $\Psi_m(\mathbf{x})$ follow the orthogonality rule $\int \int dS \psi_m(\mathbf{x}) \psi_q(\mathbf{x}) = \delta_{mq} S$ where δ_{mq} is the Kronecker delta. Using Stokes theorem to relate an area integral (over s) in two dimensions to the line integral, we have for a vector field $\mathbf{F}(\mathbf{x})$

$$\int \int ds \nabla_H \cdot \mathbf{F} = \int dl (\mathbf{F} \cdot \mathbf{n}). \quad (4.2)$$

Choosing $\mathbf{F} = \psi_q \psi_m \nabla_H \psi_n$, eqn. 4.2 leads to

$$\int \int [\psi_q (\nabla_H \psi_m \cdot \nabla_H \psi_n) + \psi_m (\nabla_H \psi_q \cdot \nabla_H \psi_n) + \psi_q \psi_m \nabla_H^2 \psi_n] ds = 0, \quad (4.3)$$

the right hand side following from the no-penetration condition at the wall. Following the same notation as Nayfeh (1987), we define,

$$\int \int ds \psi_m(\mathbf{x})\psi_n(\mathbf{x})\psi_q(\mathbf{x}) \equiv S C_{mnq}, \quad \int \int ds (\nabla_H \psi_m(\mathbf{x}) \cdot \nabla_H \psi_n(\mathbf{x})) \psi_q(\mathbf{x}) \equiv S D_{mnq}. \quad (4.4)$$

Note that $D_{nmq} = D_{mnq}$. Using 4.4, eqn. 4.3 may be written compactly as

$$D_{mnq} + D_{qnm} - k_n^2 C_{mnq} = 0. \quad (4.5)$$

Replacing $m \rightarrow n, n \rightarrow q, q \rightarrow m$ in equation 4.5, we obtain

$$D_{nqm} + D_{mqn} - k_q^2 C_{nqm} = 0. \quad (4.6)$$

which may be rewritten as

$$D_{qnm} + D_{qmn} - k_q^2 C_{nqm} = 0 \quad (4.7)$$

Using 4.7 in 4.5, we obtain

$$D_{mnq} = k_n^2 C_{mnq} - (k_q^2 C_{nqm} - D_{qmn}). \quad (4.8)$$

Replacing once again $m \rightarrow q, n \rightarrow m, q \rightarrow n$ in equation 4.5, we obtain

$$D_{qmn} + D_{nmq} - k_m^2 C_{qmn} = 0. \quad (4.9)$$

Combining 4.8 and 4.9 and the fact that $D_{mnq} = D_{nmq}$, we obtain

$$D_{nmq} = \frac{1}{2} (k_n^2 + k_m^2 - k_q^2) C_{nmq} \quad (4.10)$$

After some manipulation, expression 2.5 follows from the above expression.

Appendix B

Figs. 16 and 17 present the grid convergence results at three different grid resolutions (512^2 , 1024^2 and 2048^2) for case 4 and case 2 respectively in table 1. Figs. 18 presents the grid convergence results for fig. 13.

REFERENCES

- BASAK, S., FARSOIYA, P. K. & DASGUPTA, R. 2021 Jetting in finite-amplitude, free, capillary-gravity waves. *J. Fluid Mech.* **909**.
- BENJAMIN, T. B. & FEIR, J. E. 1967 The disintegration of wave trains on deep water part 1. theory. *J. Fluid Mech.* **27** (3), 417–430.
- BRITANNICA, THE EDITORS OF ENCYCLOPAEDIA 2024 Agulhas current. <https://www.britannica.com/place/Agulhas-Current>.
- BROWN, MICHAEL G & JENSEN, ATLE 2001 Experiments on focusing unidirectional water waves. *Journal of Geophysical Research: Oceans* **106** (C8), 16917–16928.
- CHARLIE WOOD 2020 The grand unified theory of rogue waves. <https://www.quantamagazine.org/the-grand-unified-theory-of-rogue-waves-20200205/>.
- CHAVARRIA, GERARDO RUIZ, LE GAL, PATRICE & LE BARS, MICHAEL 2018 Geometrical focusing of surface waves. *Physical Review Fluids* **3** (9), 094803.
- DAVIS, MC & ZARNICK, ERNEST E 1964 Testing ship models in transient waves. In *5th Symposium on Naval Hydrodynamics*, , vol. 507.
- DEIKE, L. 2022 Mass transfer at the ocean–atmosphere interface: the role of wave breaking, droplets, and bubbles. *Annu. Rev. Fluid Mech.* **54**, 191–224.

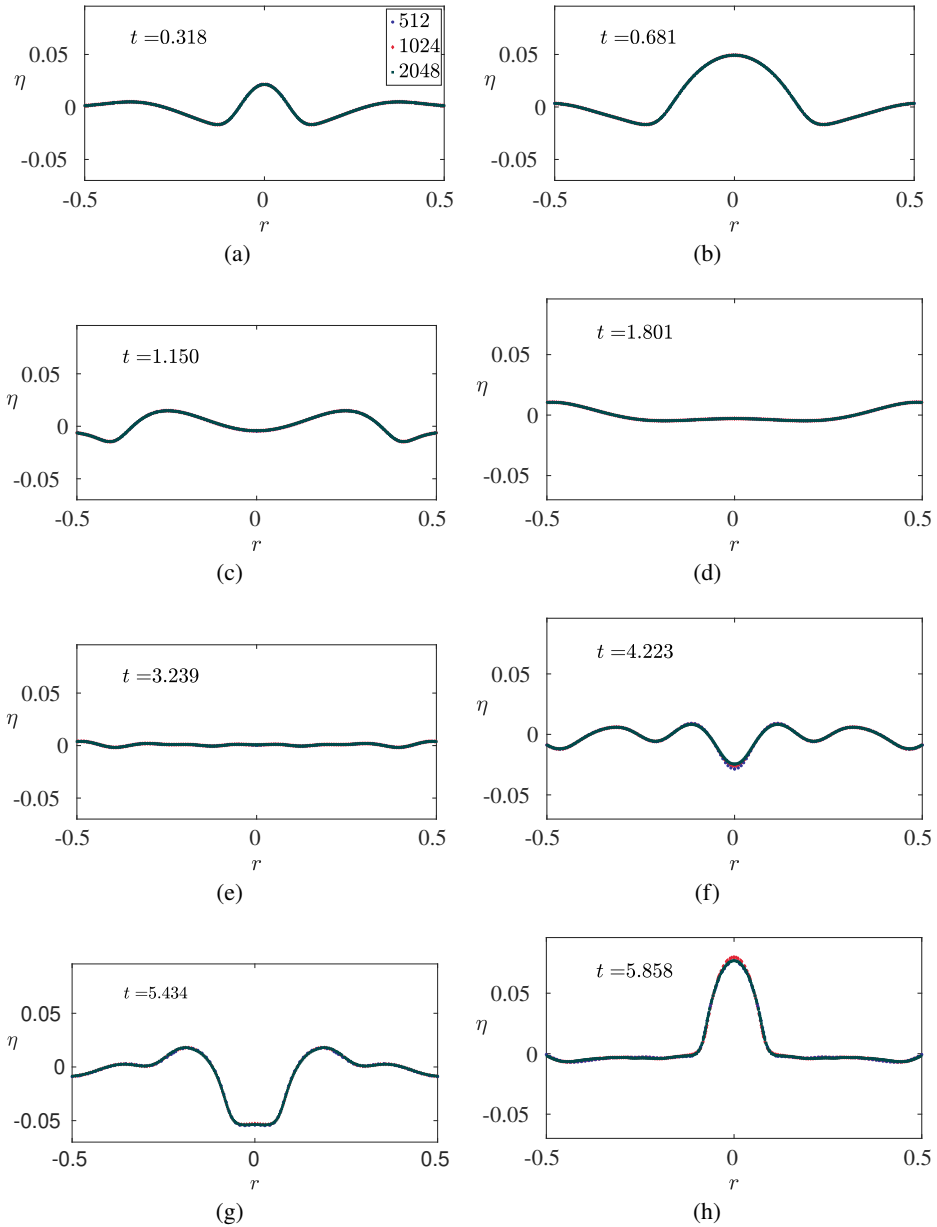


Figure 16: Comparison of interface profile for case 4 in table 1 at three different grid resolutions, 512^2 (blue dots), 1024^2 (red dots) and 2048^2 (green dots)

- DHOTE, YASHIKA, KUMAR, ANIL, KAYAL, LOHIT, GOSWAMI, PARTHA SARATHI & DASGUPTA, RATUL 2024 Standing waves and jets on a sessile, incompressible bubble. *Physics of Fluids* **36** (1).
- DUBRULLE, B. 2019 Beyond Kolmogorov cascades **867**.
- DUCHEMIN, LAURENT, POPINET, STÉPHANE, JOSSEMERAND, CHRISTOPHE & ZALESKI, STÉPHANE 2002 Jet formation in bubbles bursting at a free surface. *Physics of fluids* **14** (9), 3000–3008.
- DYSTHE, KRISTIAN, KROGSTAD, HARALD E & MÜLLER, PETER 2008 Oceanic rogue waves. *Annu. Rev. Fluid Mech.* **40**, 287–310.
- EGGERS, J. 2018 Role of singularities in hydrodynamics **3** (11), 110503.

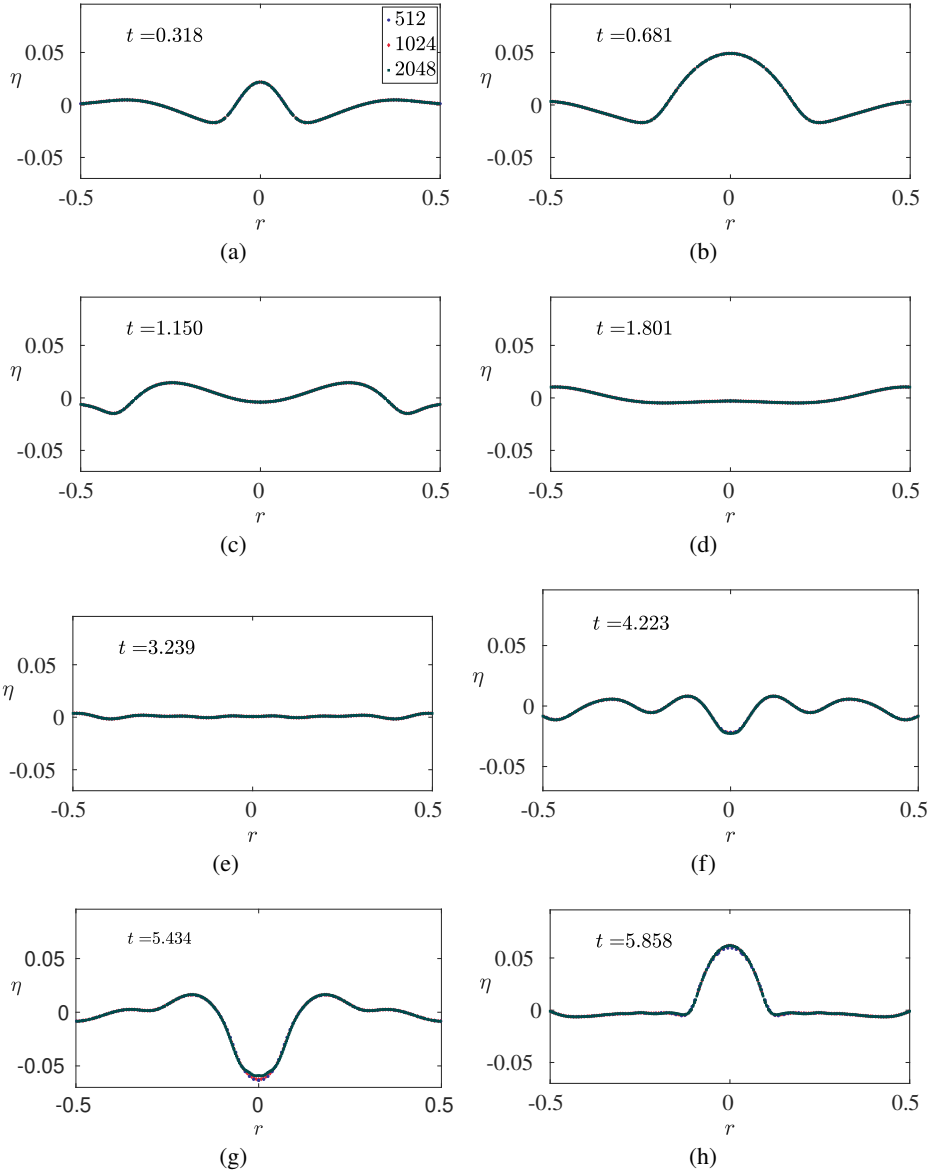


Figure 17: Comparison of interface profile for case 2 in table 1 for three different grid resolutions, 512^2 (blue dots), 1024^2 (red dots) and 2048^2 (green dots)

- EGGERS, J. G., SPRITTLER, J. & SNOEIJER, J. H. 2024 Coalescence dynamics. *Annu. Rev. Fluid Mech.* .
- FARSOIYA, PALAS KUMAR, MAYYA, YS & DASGUPTA, RATUL 2017 Axisymmetric viscous interfacial oscillations—theory and simulations. *Journal of Fluid Mechanics* **826**, 797–818.
- GHABACHE, ELISABETH, ANTKOWIAK, ARNAUD, JOSSE RAND, CHRISTOPHE & SÉON, THOMAS 2014a On the physics of fizziness: How bubble bursting controls droplets ejection. *Physics of Fluids* **26** (12).
- GHABACHE, ÉLISABETH, SÉON, THOMAS & ANTKOWIAK, ARNAUD 2014b Liquid jet eruption from hollow relaxation. *Journal of fluid mechanics* **761**, 206–219.
- GORDILLO, J. M. & BLANCO-RODRÍGUEZ, F. J. 2023 Theory of the jets ejected after the inertial collapse of cavities with applications to bubble bursting jets. *Phys. Rev. Fluids* **8** (7), 073606.

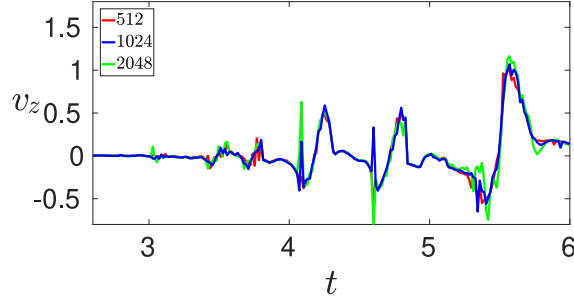
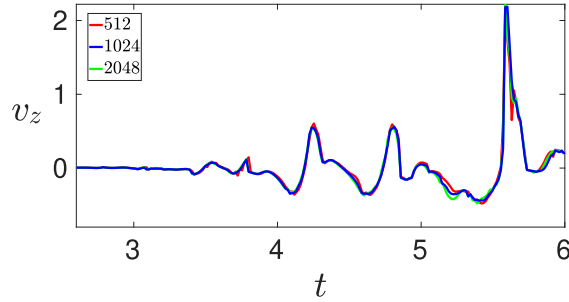
(a) $Oh = 0$ (b) $Oh = 1.17 \times 10^{-4}$

Figure 18: Comparison of the vertical velocity for case 2 (panel a) and case 4 (panel b) for three different grid resolutions, 512^2 (red solid line), 1024^2 (blue solid line) and 2048^2 (green solid line).

- HASSELMANN, K. 1962 On the non-linear energy transfer in a gravity-wave spectrum part 1. general theory. *Journal of Fluid Mechanics* **12** (4), 481–500.
- HENRI COHEN, FERNANDO RODRIGUEZ VILLEGAS & ZAGIER, DON 2000 Convergence acceleration of alternating series. *Experimental Mathematics* **9** (1), 3–12.
- JOHANNESSEN, THOMAS B & SWAN, CHRIS 2001 A laboratory study of the focusing of transient and directionally spread surface water waves. *Proceedings of the Royal Society of London. Series A: Mathematical, Physical and Engineering Sciences* **457** (2008), 971–1006.
- JOSEPH, DANIEL D 2006 Potential flow of viscous fluids: Historical notes. *International Journal of Multiphase Flow* **32** (3), 285–310.
- KAYAL 2024 Codes for cavity evolution. <https://github.com/Lohittitas/concentricWave>.
- KAYAL, LOHIT, BASAK, SASWATA & DASGUPTA, RATUL 2022 Dimples, jets and self-similarity in nonlinear capillary waves. *Journal of Fluid Mechanics* **951**, A26.
- KAYAL, LOHIT & DASGUPTA, RATUL 2023 Jet from a very large, axisymmetric, surface-gravity wave. *Journal of Fluid Mechanics* **975**, A22.
- KIENTZLER, CF, ARONS, ARNOLD B, BLANCHARD, DUNCAN C & WOODCOCK, AHHTTPS 1954 Photographic investigation of the projection of droplets by bubbles bursting at a water surface. *Tellus* **6** (1), 1–7.
- LONGUET-HIGGINS, MS 1974 Breaking waves in deep or shallow water. In *Proc. 10th Conf. on Naval Hydrodynamics*, , vol. 597, p. 605. MIT.
- LONGUET-HIGGINS, MICHAEL S 1983 Bubbles, breaking waves and hyperbolic jets at a free surface. *Journal of Fluid Mechanics* **127**, 103–121.
- LONGUET-HIGGINS, MICHAEL S 1990 An analytic model of sound production by raindrops. *Journal of Fluid Mechanics* **214**, 395–410.
- MACINTYRE, FERREN 1968 Bubbles. boundary-layer” microtome” for micronthick samples of a liquid surface. *The Journal of Physical Chemistry* **72** (2), 589–592.

- MACINTYRE, FERREN 1972 Flow patterns in breaking bubbles. *Journal of Geophysical Research* **77** (27), 5211–5228.
- MALLORY, JOHN KENNAWAY 1974 Abnormal waves on the south east coast of south africa. *The International hydrographic review* .
- MCALLISTER, ML, DRAYCOTT, S, DAVEY, T, YANG, Y, ADCOCK, TAA, LIAO, S & VAN DEN BREMER, TS 2022 Wave breaking and jet formation on axisymmetric surface gravity waves. *Journal of Fluid Mechanics* **935**.
- MCIVER, MAUREEN 1985 Diffraction of water waves by a moored, horizontal, flat plate. *Journal of Engineering Mathematics* **19** (4), 297–319.
- MEI, CC & LIU, LF 1973 The damping of surface gravity waves in a bounded liquid. *Journal of Fluid Mechanics* **59** (2), 239–256.
- MILES, JOHN W 1968 The cauchy–poisson problem for a viscous liquid. *Journal of Fluid Mechanics* **34** (2), 359–370.
- MILES, JOHN W. 1976 Nonlinear surface waves in closed basins. *Journal of Fluid Mechanics* **75** (3), 419–448.
- MOORE, D. W. 1963 The boundary layer on a spherical gas bubble. *J. Fluid Mech.* **16** (2), 161–176.
- MPMATH 2023 *mpmath: a Python library for arbitrary-precision floating-point arithmetic (version 1.3.0)*. <http://mpmath.org/>.
- MURASHIGE, SUNAO & KINOSHITA, TAKESHI 1992 An ideal ocean wave focusing lens and its shape. *Applied ocean research* **14** (5), 275–290.
- NAYFEH, ALI H 1987 Surface waves in closed basins under parametric and internal resonances. *The Physics of fluids* **30** (10), 2976–2983.
- OGUZ, HASAN N & PROSPERETTI, ANDREA 1990 Bubble entrainment by the impact of drops on liquid surfaces. *Journal of Fluid Mechanics* **219**, 143–179.
- ONORATO, MIGUEL, RESIDORI, S, BORTOLOZZO, U, MONTINA, A & ARECCHI, FT 2013 Rogue waves and their generating mechanisms in different physical contexts. *Physics Reports* **528** (2), 47–89.
- ONSAGER, L. 1949 Statistical hydrodynamics. *Il Nuovo Cimento* **6** (2), 279–287.
- PEREGRINE, D HOWELL 1976 Interaction of water waves and currents. *Advances in applied mechanics* **16**, 9–117.
- PEREGRINE, D. H. 1986 Approximate descriptions of the focussing of water waves. In *Coastal Engineering 1986*, pp. 675–685. ASCE.
- POPINET, S. & COLLABORATORS 2013–2024 Basilisk C: volume of fluid method. <http://basilisk.fr> (Last accessed: August 23, 2023).
- PRANDTL, L. 1904 Über flüssigkeitsbewegung bei sehr kleiner reibung. *Math-Kongr, Heidelberg* pp. 484–491.
- PROSPERETTI, A. 1976 Viscous effects on small-amplitude surface waves. *Phys. Fluids* **19** (2), 195–203.
- PROSPERETTI, ANDREA 1981 On the motion of two superposed viscous fluids .
- RACKAUCKAS, CHRISTOPHER & NIE, QING 2019 Confederated modular differential equation apis for accelerated algorithm development and benchmarking. *Advances in Engineering Software* **132**, 1–6.
- RACKAUCKAS, CHRISTOPHER, NIE, QING & COLLABORATORS 2017 Differentialequations.jl—a performant and feature-rich ecosystem for solving differential equations in julia. *Journal of Open Research Software* **5** (1), 15.
- RAPP, RONALD JAMES & MELVILLE, W KENDALL 1990 Laboratory measurements of deep-water breaking waves. *Philosophical Transactions of the Royal Society of London. Series A, Mathematical and Physical Sciences* **331** (1622), 735–800.
- SANJAY, V. 2022 Viscous Free-Surface Flows. PhD thesis, University of Twente.
- SANJAY, VATSAL, CHANTELOT, PIERRE & LOHSE, DETLEF 2023 When does an impacting drop stop bouncing? *Journal of Fluid Mechanics* **958**, A26.
- SANJAY, V., LOHSE, D. & JALAAL, M. 2021 Bursting bubble in a viscoplastic medium. *J. Fluid Mech.* **922**, A2.
- SANJAY, V., SEN, U., KANT, P. & LOHSE, D. 2022 Taylor-Culick retractions and the influence of the surroundings **948**, A14.
- SMITH, RONALD 1976 Giant waves. *Journal of Fluid Mechanics* **77** (3), 417–431.
- STAMNES, JAKOB J, LØVHAUGEN, ODD, SPELKAVIK, BJØSRN, MEI, CHIANG C, LO, EDMOND & YUE, DICK KP 1983 Nonlinear focusing of surface waves by a lens—theory and experiment. *Journal of Fluid Mechanics* **135**, 71–94.
- STUHLMAN JR, OTTO 1932 The mechanics of effervescence. *Physics* **2** (6), 457–466.

- TORRES, THEO, LLOYD, MAX, DOLAN, SAM R & WEINFURTNER, SILKE 2022 Wave focusing by submerged islands and gravitational analogues. *Physical Review Research* **4** (3), 033210.
- VILLERMAUX, E., WANG, X. & DEIKE, L. 2022 Bubbles spray aerosols: Certitudes and mysteries. *PNAS Nexus* **1** (5), pgac261.
- WHITE, BENJAMIN S & FORNBERG, BENGT 1998 On the chance of freak waves at sea. *Journal of fluid mechanics* **355**, 113–138.
- WU, CHIN H & NEFF, HM 2002 Breaking criteria and energy losses for three-dimensional wave breaking. *Journal of Geophysical Research: Oceans* **107** (C10), 41–1.
- XU, CHANG & PERLIN, MARC 2023 Parasitic waves and micro-breaking on highly nonlinear gravity–capillary waves in a convergent channel. *Journal of Fluid Mechanics* **962**, A46.
- ZAKHAROV, VLADIMIR E, DYACHENKO, ALEXANDER I & PROKOFIEV, ALEXANDER O 2006 Freak waves as nonlinear stage of stokes wave modulation instability. *European Journal of Mechanics-B/Fluids* **25** (5), 677–692.
- ZHU, QIANG, LIU, YUMING & YUE, DICK KP 2003 Three-dimensional instability of standing waves. *Journal of Fluid Mechanics* **496**, 213–242.